

Temporal Evolution of Prompt GRB Polarization

Ramandeep Gill^{1,2,3★}, Jonathan Granot^{2,3,1†}

¹Department of Physics, The George Washington University, Washington, DC 20052, USA

²Department of Natural Sciences, The Open University of Israel, P.O. Box 808, Ra'anana 43537, Israel

³Astrophysics Research Center of the Open university (ARCO), The Open University of Israel, P.O. Box 808, Ra'anana 43537, Israel

Accepted XXX. Received YYY; in original form ZZZ

ABSTRACT

The dominant radiation mechanism that produces the prompt emission in gamma-ray bursts (GRBs) remains a major open question. Spectral information alone has proven insufficient in elucidating its nature. Time-resolved linear polarization has the potential to distinguish between popular emission mechanisms, e.g., synchrotron radiation from electrons with a power-law energy distribution or inverse Compton scattering of soft seed thermal photons, which can yield the typical GRB spectrum but produce different levels of polarization. Furthermore, it can be used to learn about the outflow's composition (i.e. whether it is kinetic-energy-dominated or Poynting-flux-dominated) and angular structure. For synchrotron emission it is a powerful probe of the magnetic field geometry. Here we consider synchrotron emission from a thin ultrarelativistic outflow, with bulk Lorentz factor $\Gamma(R) = \Gamma_0(R/R_0)^{-m/2} \gg 1$, that radiates a Band-function spectrum in a single (multiple) pulse(s) over a range of radii, $R_0 \leq R \leq R_0 + \Delta R$. Pulse profiles and polarization evolution at a given energy are presented for a coasting ($m = 0$) and accelerating ($m = -2/3$) thin spherical shell and for different viewing angles for a top-hat jet with sharp as well as smooth edges in emissivity. Four different magnetic field configurations are considered, such as a locally ordered field coherent over angular scales $\theta_B \gtrsim 1/\Gamma$, a tangled field (B_\perp) in the plane transverse to the radial direction, an ordered field (B_\parallel) aligned in the radial direction, and a globally ordered toroidal field (B_{tor}). All field configurations produce distinct polarization evolution with single (for B_\perp and B_\parallel) and double (for B_{tor}) 90° changes in the polarization position angle.

Key words: radiation mechanisms: non-thermal – relativistic processes – magnetic fields – polarization – gamma-ray burst: general

1 INTRODUCTION

The non-thermal prompt gamma-ray burst (GRB) spectrum is generally described by the empirical Band function (Band et al. 1993) that features a smoothly broken power law. In rare cases deviations from the Band spectrum have also been found where the spectrum, e.g., appears to be quasi-thermal (e.g., Ryde 2004, 2005), features a thermal component in addition to the non-thermal Band component (e.g., Guiriec et al. 2011, 2017), shows a low-energy spectral break (Oganesyan et al. 2017; Ravasio et al. 2018, 2019), and a high-energy break usually interpreted as due to $\gamma\gamma$ -annihilation (e.g., Ackermann et al. 2013; Tang et al. 2015; Vianello et al. 2018). The νF_ν spectrum peaks at a mean energy of $\langle E_{\text{pk}} \rangle \simeq 250$ keV, around which most of the energy in the burst comes out. Theoretical efforts focused on understanding the origin of this spectrum over the last few decades (see reviews by Piran 2004; Kumar & Zhang 2015) have narrowed it down to two popular radiative mechanisms – synchrotron emission from power law electrons (Sari & Piran 1997; Daigne & Mochkovitch 1998) and inverse-Compton scattering by mildly relativistic electrons on soft seed thermal photons operating in both optically thick and thin emission regions (Thompson 1994;

Ghisellini & Celotti 1999; Giannios 2006; Thompson & Gill 2014; Gill & Thompson 2014; Vurm & Beloborodov 2016).

Both mechanisms are able to explain the typical prompt GRB spectrum, although there are exceptional cases where some spectral features are more naturally explained by one or the other. For example, the canonical optically-thin synchrotron emission model is disfavoured in bursts that show low-energy spectral slopes harder than the so-called synchrotron line-of-death, with $d \ln F_\nu / d \ln \nu > 1/3$ (e.g., Crider et al. 1997; Preece et al. 1998; Ghirlanda et al. 2003). Harder low-energy spectral slopes have been accommodated using this model if the magnetic field gradually declines in the emission region as the flow expands (Uhm & Zhang 2014; Geng et al. 2018). Alternatively, these can be explained with sub-photospheric dissipation models that feature a quasi-thermal spectral peak broadened by Comptonization (e.g. Vurm & Beloborodov 2016; Beloborodov & Mészáros 2017). Sub-photospheric dissipation models sometimes also produce double-hump spectra (Guiriec et al. 2011, 2017) where the quasi-thermal component produces the νF_ν -peak and the non-thermal component dominates the spectrum at energies above and below E_{pk} ; in some very rare cases more than two spectral components have also been shown to fit the prompt GRB spectrum (Guiriec et al. 2015). The double-hump spectrum has been shown (Gill et al. 2020a) to arise in a sub-photospheric dissipation model by power-law electrons emitting synchrotron photons (Beniamini & Giannios 2017) or gradually heated mono-energetic electrons cool-

★ E-mail: rsgill.rg@gmail.com

† E-mail: granot@openu.ac.il

ing on soft seed thermal photons via Comptonization (e.g., [Giannios 2008](#)). This degeneracy between the two emission mechanisms has lead to a deadlock hindering further progress on understanding, e.g., the composition – kinetic energy dominated or Poynting flux dominated – of the ultrarelativistic outflow as well as the particle acceleration/heating mechanisms since both of these ultimately dictate the dominant radiation process.

One promising way to break this degeneracy is the measurement of linear polarization (Π) which would strongly favour synchrotron emission if $\Pi \gtrsim 20\%$ is measured in most GRBs ([Gill et al. 2020a](#)). In general, negligible polarization is expected from a Comptonized spectrum since multiple scatterings tend to wash out any preferred direction of the polarization vector. However, if an axisymmetric flow has an angular structure, in particular with a steep gradient in the bulk Lorentz factor $\Gamma(\theta)$ with polar angle θ measured from the jet symmetry axis, Comptonized emission can yield $\Pi \lesssim 20\%$ (e.g., [Ito et al. 2014](#); [Lundman et al. 2014](#); [Parsotan et al. 2020](#)). Therefore, apart from helping in determining the dominant radiation mechanism for the prompt emission, linear polarization is also a valuable tool for understanding the jet’s angular structure. What is more, in the case of synchrotron emission, since different magnetic field configurations produce different levels of polarization for a given jet geometry, observer’s line-of-sight (LOS), and spectral index, linear polarization measurements can potentially constrain the magnetic field geometry in the emission region (e.g. as was done for the afterglow phase in [Gill & Granot 2020](#)). For example, even a single statistically significant measurement of polarization at the level of $50\% \lesssim \Pi \lesssim 60\%$ will definitively indicate the presence of an ordered magnetic field, such as a globally ordered toroidal field ([Gill et al. 2020a](#)).

Thus far, linear polarization measurements of prompt GRB emission (see, e.g., Table 1 of [Gill et al. 2020a](#)) have not been able to settle this issue. Even though several such measurements exist, they are of low statistical significance ($\lesssim 3\sigma$) and the results are inconsistent when compared between different detectors. Measurements by IKAROS-GAP ([Yonetoku et al. 2011, 2012](#)) and AstroSat-CZTI ([Chand et al. 2018](#); [Chattopadhyay et al. 2019](#); [Chand et al. 2019](#); [Sharma et al. 2019](#)) tentatively find high levels of polarization with $\Pi \gtrsim 50\%$. However, time-integrated measurements obtained by POLAR ([Zhang et al. 2019](#); [Burgess et al. 2019](#); [Kole et al. 2020](#)) yield low-levels of polarization with $\Pi \lesssim 20\%$ instead, with most GRBs consistent with being unpolarized within the 2σ confidence level. On the other hand, their time-resolved analysis did find moderate polarization with a time-varying polarization position angle (PA) for GRB 170114A. If this is indeed the case, then a time-integrated analysis would indeed yield very low polarization since it is being averaged out by the variation of the PA. This calls for a more careful time-resolved polarization analysis of bright GRBs and comparison of the measured polarization with time-resolved theoretical estimates.

Detailed treatments of energy-independent linear polarization from synchrotron emission in ultrarelativistic GRB jets have appeared in several works ([Ghisellini & Lazzati 1999](#); [Gruzinov 1999](#); [Sari 1999](#); [Granot & Königl 2003](#); [Rossi et al. 2004](#); [Granot & Taylor 2005](#)). Pulse-integrated prompt GRB polarization from synchrotron emission has been calculated for a locally ordered magnetic field in a thin spherical shell as well as for different field configurations, such as a tangled field in the plane transverse to the radial direction (B_{\perp}) and an ordered field aligned with the radial direction (B_{\parallel}), or ordered in the tangential direction (B_{ord}), in a top-hat jet in [Granot \(2003\)](#). The same for a globally ordered toroidal field in a spherical shell were presented in [Lyutikov et al. \(2003\)](#), where in the context of afterglow polarization it was also calculated for a

structured power-law jet ([Lazzati et al. 2004b](#)) and for a top-hat jet ([Granot & Taylor 2005](#)). Key results for pulse-integrated polarization from synchrotron emission and from different magnetic field configurations in a top-hat jet and their statistical incidence in a large sample of GRBs are summarized in [Toma et al. \(2009\)](#) and [Gill et al. \(2020a\)](#). The latter also discussed polarization from structured jets and alternative radiation mechanisms to synchrotron, such as non-dissipative photospheric emission ([Beloborodov 2011](#); [Lundman et al. 2014](#)) and Compton drag ([Lazzati et al. 2004a](#)).

While most works have presented pulse-integrated and energy-independent polarization results, the need for time-resolved and energy-resolved polarization models has become important only recently. Time-resolved polarization was reported for GRB 170114A ([Burgess et al. 2019](#)), a bright single pulsed GRB jointly observed by POLAR and *Fermi*-GBM, with increasing level of polarization towards the pulse peak that reached $\Pi \sim 30\%$ at the peak. This was accompanied by a time-varying PA. Time-resolved treatment of polarization of synchrotron emission from an ordered toroidal field in a coasting top-hat jet is presented in [Cheng et al. \(2020\)](#), where the magnetic field is assumed to decay with radius as a power law in a prescribed way. The power-law electron distribution, as it cools due to adiabatic, synchrotron, and synchrotron self-Compton cooling, is obtained by numerically solving the continuity equation in energy space. [Lan et al. \(2020\)](#) consider a wide variety of magnetic field configurations involving both ordered and random field components and for which they present time-integrated but energy-resolved polarization in a coasting top-hat jet.

In this work, we address the question of time-resolved prompt GRB polarization of synchrotron emission arising from physically motivated magnetic field configurations and outflow dynamics as well as angular structure. First, in §2, we calculate the polarization evolution over a single pulse using a general framework of an ultrarelativistic thin radiating shell. The comoving spectrum is described by the Band function whose νF_{ν} , spectral peak energy and normalization each evolve as a power law with radius.

In §3 synchrotron emission is assumed to be the dominant radiation mechanism for which we calculate the physically motivated scalings needed to describe the radial evolution of the spectral emissivity. Two different types of outflows are considered: (i) a kinetic-energy-dominated (KED; §3.1) coasting (constant bulk Γ) flow in which internal shocks efficiently dissipate the baryonic kinetic energy, and (ii) a Poynting-flux-dominated (PFD; §3.2) accelerating flow in which magnetic reconnection, MHD instabilities or multiple weak shocks in a variable outflow tap the magnetic field energy.

In §4 we present the formalism to calculate the time-resolved polarization over a single pulse and integrated over the observed image of the outflow on the plane of the sky. We consider four different magnetic field configurations, namely a locally ordered field (B_{ord}) with angular coherence length on the order of the angular size of the beaming cone ($\theta_B \gtrsim 1/\Gamma$), a tangled field (B_{\perp}) that lies entirely in the plane transverse to the radial direction, an ordered field aligned with the radial direction (B_{\parallel}) at each point of the outflow, and a globally ordered toroidal field (B_{tor}) that is axisymmetric around the jet symmetry axis. Results for a thin spherical shell are presented first in §4.1 both for a KED and PFD flow. This case is relevant when the beaming cone doesn’t include the edge of the jet in which case the emission appears as if it’s coming from a spherical flow. Time-resolved polarization curves for different viewing angles from a top-hat jet (§4.2) and a smooth top-hat jet (§4.3), with a uniform core and with either exponential or power-law wings, are presented next.

For GRBs that are not exceptionally bright and lack clear single pulses an integration over multiple pulses is generally performed that

Symbol	Definition
R_0	Radius at which emission turns on
ΔR	Radial distance over which shell emits continuously
R_f	Radius at which emission turns off: $R_f = R_0 + \Delta R$
\hat{R}	Normalized radius: $\hat{R} = R/R_0$
Γ_0	Bulk- Γ of emission region at R_0
t_0	Arrival time of first photons emitted along the LOS at R_0
ν_0	Observed νF_ν peak frequency of first photons emitted from R_0 along the LOS that arrived at time t_0
m	Bulk Lorentz factor PL index: $\Gamma^2 \propto R^{-m}$
ℓ	Lab-frame B-field PL index: $B \propto R^\ell$
s	Minimum particle Lorentz factor PL index: $\gamma_m \propto R^s$
a	Spectral luminosity PL index: $L'_{\nu'} \propto R^a$
d	Peak frequency PL index: $\nu'_{\text{pk}} \propto R^d$
b_1, b_2	Asymptotic Band-function spectral indices: $d \ln F_\nu / d \ln \nu$
\tilde{t}	Normalized apparent time: $\tilde{t} = t/t_0$
\tilde{t}_{pk}	Normalized pulse peak time: $\tilde{t}_{\text{pk}} = t_{\text{pk}}/t_0$
\tilde{t}_{cross}	Normalized crossing time of the Band-function break frequency $x_b = (b_1 - b_2)/(1 + b_1)$ across $x_0 = \nu/\nu_0$
$\tilde{\theta}$	Polar angle measured from the LOS
$\tilde{\xi}, \tilde{\xi}_0, \xi_j, \xi_{0,j}$	$(\Gamma\tilde{\theta})^2, (\Gamma_0\tilde{\theta})^2, (\Gamma\theta_j)^2, (\Gamma_0\theta_j)^2$
q	$\theta_{\text{obs}}/\theta_j$
Δ	Smoothing parameter for a top-hat jet with exponential wings in $L'_{\nu'}$
δ	Smoothing parameter for a top-hat jet with power-law wings in $L'_{\nu'}$
on-beam	When emission is received from within the $1/\Gamma$ beaming cone of the emitting material
off-beam	When emission is received from outside of the $1/\Gamma$ beaming cone of the emitting material

Table 1. Various symbols or terms and their definitions

can yield polarization results different from those expected for a single isolated pulse. We address this point in §5 and present results for integration over multiple pulses. Finally, we summarize this work (§6) and discuss time variation of the PA (§6.1) and energy dependence of polarization (§6.2) at the end.

2 PULSE AND SPECTRAL MODEL

We consider an ultrarelativistic ($\Gamma \gg 1$) thin shell with lab-frame width much smaller than the causal size at that radius, such that $\Delta \ll R/\Gamma^2$. This assumption is valid when the bulk of the prompt emission arises from a very thin layer, which is guaranteed when the (comoving) cooling time of electrons is much shorter than the dynamical time, $t'_{\text{cool}} \ll t'_{\text{dyn}} = R/\Gamma c$. To study the temporal evolution of the polarization we follow the treatment of Genet & Granot (2009) (also see, e.g., Uhm & Zhang 2015, 2016) and construct a simple pulse model in which the thin shell starts to radiate at $R = R_0$ and continues to radiate until $R = R_f = R_0 + \Delta R$, where the emission is assumed to be switched off abruptly. The analysis can be easily extended to more complex pulse profiles where the emission, e.g., switches off gradually (see Appendix C of Genet & Granot 2009, or Beniamini & Granot 2016), which would make the pulse peaks rounder and less spiky, but it will not alter the main results in a significant way. The radial evolution of the bulk Lorentz factor (LF) of the shell can be written generally as $\Gamma^2(R) = \Gamma_0^2(R/R_0)^{-m}$, with $\Gamma_0 = \Gamma(R_0)$, which allows for a coasting flow ($m = 0$), an accelerating flow ($m < 0$), and a decelerating flow ($m > 0$).

As the flow expands, the observed flux density, $F_\nu \propto t^{-\alpha} \nu^{-\beta}$, changes with the apparent time t due in part to the radially evol-

ing comoving (all comoving quantities henceforth are marked with a prime) isotropic-equivalent spectral luminosity and peak energy that scale as a power-law with radius,

$$L'_{\nu'}(R, \theta) = L'_0 \left(\frac{R}{R_0} \right)^a S \left(\frac{\nu'}{\nu'_{\text{pk}}} \right) f(\theta) \quad \text{with} \quad \nu'_{\text{pk}} = \nu'_0 \left(\frac{R}{R_0} \right)^d, \quad (1)$$

where $L'_0 = L'_{\nu'_{\text{pk}}}(R_0)$ and $\nu'_0 = \nu'_{\text{pk}}(R_0)$ are normalizations of the spectral luminosity and peak frequency at $R = R_0$. The factor $f(\theta)$ represents the angular structure of the emissivity normalized to unity at $\theta = 0$ with $f(0) = 1$, where θ is the polar angle measured from the jet symmetry axis. This means that $f(\theta) = 1$ for a spherical flow and $f(\theta) = \mathcal{H}(\theta_0 - \theta)$ for a top-hat jet with jet half-opening angle θ_0 and $\mathcal{H}(x)$ being the Heaviside function. Here we make the explicit assumption that the emission is isotropic in the comoving frame as well as uniform over the entire shell, and thus depends only on R . We define the normalized frequency, in terms of the peak frequency, as

$$x \equiv \frac{\nu'}{\nu'_{\text{pk}}} = \frac{\nu'}{\nu'_0} \left(\frac{R}{R_0} \right)^{-d} = \frac{\delta_D^{-1}}{(2\Gamma_0)^{-1}} \frac{\nu}{\nu_0} \left(\frac{R}{R_0} \right)^{-d} = \frac{2\Gamma_0}{\delta_D} x_0 \left(\frac{R}{R_0} \right)^{-d}. \quad (2)$$

Here we fix ν'_0 using the peak frequency of the first photons emitted along the observer's LOS from radius R_0 and that were received at time $t = t_0$, so that $\nu_0 \equiv \nu_{\text{pk}}(t_0) = \nu/x_0$ and $\nu'_0 = (1+z)\nu_0/2\Gamma_0$, where we made use of the Lorentz transformation, $\nu = \delta_D \nu'/(1+z)$ where δ_D is the Doppler factor (see §4), and the fact that $\delta_D = 2\Gamma(R) = 2\Gamma_0$ for emission along the LOS. The comoving spectrum, $S(x)$, is described by the Band-function

$$S(x) = e^{1+b_1} \begin{cases} x^{b_1} e^{-(1+b_1)x}, & x \leq x_b \\ x^{b_2} x_b^{b_1-b_2} e^{-(b_1-b_2)x}, & x \geq x_b \end{cases}, \quad (3)$$

where the break energy $x_b = (b_1 - b_2)/(1 + b_1) > 1$ when $b_2 < -1$. The local spectral index is given by $\beta \equiv -d \ln S(x)/d \ln x = x(1 + b_1) - b_1$ for $x \leq x_b$ and $\beta = -b_2$ for $x > x_b$. From the definition of x , the peak of the νF_ν spectrum occurs at $x = 1$ for which $S(x = 1) = 1$, and therefore $xS(x = 1) = 1$ at the spectral peak.

The various symbols, along with their definitions, that appear in most expressions presented in this work are collected in Table 1 for convenience.

3 SCALINGS FOR SYNCHROTRON EMISSION AND OUTFLOW DYNAMICS

The dynamics of the relativistic outflow, in particular, the radial dependence of bulk Γ can vary between different models that prescribe different compositions. Here we do not consider pair enrichment and instead assume a proton-electron plasma where the outflow composition describes the division of energy between the particles and the electromagnetic field. The composition can be characterized using the magnetization¹ $\sigma = B'^2/4\pi n' m_p c^2$, which is the ratio of the (proper) enthalpy density of the comoving magnetic field ($B'^2/4\pi$), with strength $B' = B/\Gamma \propto R^{\ell+m/2}$ where $B \propto R^\ell$ is the lab-frame magnetic field, to that of the cold baryons ($w' \approx n' m_p c^2$) with comoving number density n' . Here m_p is the proton mass and c is the speed of light. The comoving number density of electrons in the ejecta shell

¹ More generally, the specific enthalpy $h = w'/\rho' c^2$ appears in the denominator, but here we assume a cold plasma where $h \approx 1$.

scales as² $n' \propto V'^{-1} \propto (R^2\Gamma)^{-1} \propto R^{(m-4)/2}$. Therefore, the magnetization of the outflow scales as $\sigma \propto R^{(4+4\ell+m)/2}$. When $\sigma \ll 1$, most of the energy resides in the kinetic energy of the baryons, part of which is dissipated in internal shocks and then part of that is radiated. Alternatively, when $\sigma > 1$, the outflow is Poynting flux dominated and the main energy reservoir is the magnetic field. The dynamics of the flow are different in both scenarios.

Here we assume that synchrotron emission, arising from power-law electrons gyrating in the shock-generated magnetic field or that advected from the base of the flow, forms the dominant radiation component that produces the Band-like spectra of GRBs. In order to ensure a high radiative efficiency, the electrons must be in the fast-cooling regime (Sari et al. 1998), so that $\nu'_c < \nu'_m$ where $\nu'_c \propto (B'^3 t_{\text{dyn}}^2)^{-1} \propto R^{-(5m+6\ell+4)/2}$ is the characteristic cooling break frequency, with $t'_{\text{dyn}} \sim R/\Gamma c \propto R^{(m+2)/2}$ being the comoving dynamical time, and $\nu'_m \propto B' \gamma_m^2 \propto R^{(2\ell+m+4s)/2}$ is the synchrotron radiation frequency of minimal energy electrons with LF $\gamma_m \propto R^s$. The νF_ν synchrotron spectrum peaks at $\nu_{\text{pk}} \propto \Gamma \nu'_m \propto R^{\ell+2s}$ in the central engine frame, making it the characteristic frequency at which most of the energy of the burst comes out. The number of electrons emitting synchrotron photons at the peak luminosity and occupying the causal volume $\tilde{V}' \propto R^3/\Gamma \propto R^{(6+m)/2}$ are $N_e = n' \tilde{V}' \propto R^{1+m}$. The comoving spectral luminosity at the peak frequency is obtained from $L'_{\nu_{\text{pk}}} = L'_{\nu'_{\text{max}}} (\nu'_m/\nu'_c)^{-1/2} \propto R^{-(\ell+s)}$, where the maximum spectral luminosity can be approximated by using the synchrotron power emitted by the electron, P'_{syn} , at the characteristic synchrotron frequency, $L'_{\nu'_{\text{max}}} \sim N_e P'_{\text{syn}}/\nu \propto N_e B' \propto R^{(2\ell+2\ell+3m)/2}$. From the above discussion we find the power-law indexes of the spectral luminosity and peak energy in Eq. (1) to be

$$a = -(\ell + s) \quad \text{and} \quad d = \ell + 2s + m/2. \quad (4)$$

3.1 Kinetic Energy Dominated Flow: Internal Shocks

The temporal variability of GRB lightcurves, with variability timescale $t_v \sim 10^{-3} - 1$ s (Fishman & Meegan 1995), can be understood using the internal shocks model (Rees & Meszaros 1994; Paczynski & Xu 1994; Sari & Piran 1997; Daigne & Mochkovitch 1998), which posits that the observed variability reflects that of the central engine. Variability in long-soft GRBs can also be embedded in the flow as the jet traverses the stellar envelope due to pressure confinement, mixing, and shocks (e.g. Matzner 2003). A similar situation can arise in the prompt emission of short-hard GRBs where the jet breaks out of the circum-merger ejecta. Here we consider the canonical scenario where the central engine accretes intermittently and ejects shells of matter that are initially separated by length scale $\sim ct_v/(1+z)$ and have fluctuations in bulk LFs of order $\Delta\Gamma \sim \Gamma$, the mean bulk LF of the unsteady flow. As a result, after the outflow acceleration saturates with $\Gamma(R) = \Gamma_\infty \propto R^0$, and therefore $m = 0$, faster moving shells catch up from behind with slower ones and collide with each other to dissipate their kinetic energy at internal shocks that occur at the dissipation radius $R_{\text{dis}} = 2\Gamma_\infty^2 ct_v/(1+z) = 6 \times 10^{13} (1+z)^{-1} \Gamma_{\infty,2}^2 t_{v,-1}$ cm for a source at redshift z .

² More generally, $V' \propto R^2 \Delta'$ where $\Delta' = \Gamma \Delta$ and $\Delta \approx \max(\Delta_0, R/\Gamma^2)$, so the expression here holds only before the spreading radius, $R < R_\Delta \approx \Delta_0 \Gamma^2 (R_\Delta)$, where $\Delta_0 \approx ct_{\text{GRB}}/(1+z)$ is the radial width of the outflow and T_{GRB} is the total GRB duration. The dissipation radius is typically $R_{\text{dis}} \lesssim \Gamma^2 (R_{\text{dis}}) ct_v/(1+z)$ where $t_v < T_{\text{GRB}}$ is the variability time, so that $[R_{\text{dis}}/\Gamma^2 (R_{\text{dis}})]/[R_\Delta/\Gamma^2 (R_\Delta)] \lesssim t_v/T_{\text{GRB}} \ll 1$ and indeed $R_{\text{dis}} \ll R_s$ since R/Γ^2 typically increases with R (i.e. $m > -1$).

In each collision between two adjacent shells a double shock structure forms, with forward and reverse shocks going into the slower and faster shells, respectively, which shock heat a fraction ξ_e of the electrons into a power-law energy distribution, $dN_e/d\gamma_e \propto \gamma_e^{-p}$ for $\gamma_e > \gamma_m$, which holds a fraction ϵ_e of the total internal energy density behind the shock. Here $\gamma_m = [(p-2)/(p-1)](\epsilon_e/\xi_e)(m_p/m_e)(\Gamma_{\text{ud}} - 1)$ is the LF of minimal energy electrons, where m_p and m_e are the proton and electron masses. The strength of the two shocks is characterized by the relative upstream to downstream LF³, Γ_{ud} , which is expected to be roughly constant with radius for the simplest case of two uniform shells, as considered here. In this case, the LF of minimal energy electrons, $\gamma_m \propto R^0$, remains independent of radius, and therefore $s = 0$.

In a coasting flow, the radial size of a given fluid element remains constant, but its transverse size increases with radius. Consequently, magnetic flux conservation yields the scaling $B_r \propto R^{-2}$ for the radial component of the magnetic field and $B_{\theta,\phi} \propto R^{-1}$ for the transverse components. Energy is dissipated at a radial distance much larger than that where the flow bulk- Γ saturates, such that $R_{\text{dis}}/R_s = 2\Gamma_\infty ct_v/R_\ell \gg 1$, where $R_s = \Gamma_\infty R_\ell$ is the saturation radius for a fireball expanding under its own pressure and R_ℓ is the jet launching radius. A similar situation can arise even in initially Poynting-flux-dominated highly variable flows (Granot et al. 2011; Granot 2012; Komissarov 2012) for which the magnetization declines with radius, $\sigma(R) \propto R^{-1/3}$. Once the flow transitions to being weakly magnetized, with $\sigma < 1$ at $R > R_s \sim \Gamma_\infty^2 ct_v \sim R_{\text{dis}}$ where the saturation radius in this scenario is defined below, internal shocks again become efficient at dissipating energy. In both scenarios, the transverse component of the magnetic field dominates, which yields $B \propto R^{-1}$ and $\ell = -1$.

For the internal shock model in a KED flow, we find that $a = 1$ and $d = -1$.

3.2 Poynting Flux Dominated Flow: Magnetic Reconnection

An attractive alternative to internal shocks is the possibility that the relativistic outflow is permeated by strong magnetic fields advected from the base of the flow at $R = R_\ell$ (e.g., Thompson 1994; Lyutikov & Blandford 2003). Since $\sigma > 1$ in this scenario, internal shocks are rendered inefficient in dissipating any kinetic energy of the flow. Instead, the main energy reservoir is the magnetic field, which is dissipated due to magnetic reconnection and/or MHD instabilities, e.g. the Kruskal-Schwarzschild instability (Lyubarsky 2010; Gill et al. 2018) which is the magnetic analog of the Rayleigh-Taylor instability. A popular model of a PFD outflow is that of a striped-wind (Lyubarsky & Kirk 2001; Spruit et al. 2001; Drenkhahn 2002; Drenkhahn & Spruit 2002; Bégué et al. 2017) where the magnetic field lines reverse polarity over a characteristic length scale $\lambda \sim \pi R_L = \pi c/\Omega = cP/2 = 1.5 \times 10^7 P_{-3}$ cm. Here R_L is the light cylinder radius, $\Omega = 2\pi/P$ is the central engine's rotational angular frequency, and $P = 10^{-3} P_{-3}$ s is its spin period. While this parameterization is relevant for a millisecond magnetar (e.g., Metzger et al. 2011), more generally, stochastic polarity flips in the outflow launched by a BH have $\lambda \gtrsim R_L$ (McKinney & Uzdensky 2012; Parfrey et al. 2015). Magnetic energy is dissipated as opposite polarity field lines are brought together at the inflow plasma velocity $v_{\text{in}} = \epsilon v_A$, where $\epsilon \sim 0.1$ and $v_A \simeq c$ is the Alfvén

³ $\Gamma_{\text{ud}} \cong \frac{1}{2}(\Gamma_u/\Gamma_d + \Gamma_d/\Gamma_u)$ is the LF of the upstream (unshocked) material moving with LF $\Gamma_u \gg 1$ as measured in the frame of the downstream (shocked) material moving with LF $\Gamma_d \gg 1$.

speed which approaches the speed of light c when $\sigma \gg 1$, and undergo reconnection. A significant fraction of the dissipated energy goes towards accelerating the flow with $\Gamma \propto R^{1/3}$ ($m = -2/3$) for $R_A < R < R_s$, where $R_A \sim \text{few} \times R_L$ is the Alfvén radius and $R_s = \Gamma_\infty^2 \lambda / 6\epsilon = 1.7 \times 10^{13} \Gamma_\infty^2 (\lambda/\epsilon)_8 \text{ cm}$ is the saturation radius. The latter defines the radial distance beyond which no magnetic dissipation occurs and the flow starts to coast at $\Gamma = \Gamma_\infty$.

Broadly similar flow dynamics and energy dissipation is obtained in a highly variable magnetized outflow (Granot et al. 2011; Granot 2012; Komissarov 2012) that doesn't require magnetic field polarity reversals to dissipate energy at reconnection sites. Instead, energy is dissipated in multiple weak internal shocks that operate at $R \ll R_s$ when $\sigma \gg 1$. These shocks gradually become more efficient as the magnetization declines and become strongest and most efficient when $\sigma \lesssim 1$ for $R \gtrsim R_s$. In this case λ/c is the variability time of the outflow emanating from the central source.

For an axisymmetric magnetic field, such as a globally toroidal field centered on the jet symmetry axis, the poloidal component declines faster, with $B_p \propto R^{-2}$, as compared to the toroidal component that scales as $B_\phi \propto R^{-1}$. Therefore, at large distances from the central engine, where dissipation occurs and detectable non-thermal emission is produced, the toroidal component dominates, which again yields $\ell = -1$.

To determine the scaling of γ_m with radius, we consider the mean energy per baryon which cannot exceed $\sigma m_p c^2$ as this is the total dissipated energy per baryon-electron for complete magnetic dissipation. A fraction of the dissipated energy is deposited in the electrons and their mean energy per particle, $\langle \gamma_e \rangle$, scales with that of the protons. Since $\gamma_m \propto \langle \gamma_e \rangle \propto \sigma$, which yields $s = (4 + 4\ell + m)/2 = -1/3$. This is strictly valid for $p > 2$ for which most of the energy resides near γ_m . However, many works find that the power-law index $p = p(\sigma)$ depends sensitively on σ , where the dependence can be approximately expressed as $p = 4\sigma^{-0.3}$ (Sironi & Spitkovsky 2014; Guo et al. 2015; Kagan et al. 2015; Werner et al. 2016). As a result, $p < 2$ for $\sigma > 10$ in which case most of the energy in particles starts shifting towards larger particle LFs, $\gamma_e \gg \gamma_m$. What's relevant here is the value of σ when the flow becomes optically thin so that radiation can stream out. Gill et al. (2020b) carried out numerical simulations of a PFD flow over a range of dissipation radii and in all cases of interest here $\sigma < 10$ in the optically thin parts of the flow. Therefore, we find that the scaling of γ_m is reasonably justified.

For the PFD flow with a striped wind magnetic field structure, we find that $a = 4/3$ and $d = -2$.

4 LINEAR POLARIZATION OVER A SINGLE PULSE

Synchrotron emission, in general, is partially linearly polarized. Its anisotropic emissivity and local (for a given point on the surface of the outflow) polarization depends on the direction of the magnetic field with respect to the observer's LOS in the comoving frame. The direction of the polarization vector, $\hat{\Pi}' = (\hat{n} \times \hat{B})/|\hat{n} \times \hat{B}|$, is always transverse to both \hat{n} , the unit vector pointing along the LOS (the direction of a photon that reaches the observer), and \hat{B} , the unit vector pointing in the local direction of the magnetic field, regardless of the Lorentz frame. While the magnitude of local polarization remains Lorentz invariant, its direction in the observer frame is obtained with appropriate Lorentz transformations. Since synchrotron emission arising from different fluid elements is incoherent, the total polarization is obtained by taking a ratio of the total polarized intensity to the total intensity, where both are integrated over the entire image of the outflow as observed on the plane of the sky.

Here we first present a formalism valid for a spherical shell. We later generalize it to cover other outflow structures, namely a top-hat jet and a uniform jet with smooth edges in emissivity.

The flux density measured by a distant observer in the direction of the unit vector \hat{n} from an infinitely 'thin-shell' at an apparent time t for a source at redshift z with luminosity distance $d_L(z)$ is given by (Granot 2005)

$$F_\nu(t) = \frac{(1+z)}{16\pi^2 d_L^2} \int \delta_D^3 L'_\nu d\tilde{\Omega}, \quad (5)$$

where $\delta_D = [\Gamma(1 - \vec{\beta} \cdot \hat{n})]^{-1} = [\Gamma(1 - \beta \tilde{\mu})]^{-1}$ is the Doppler factor, $\hat{n} \cdot \vec{\beta} \equiv \tilde{\mu} = \cos \tilde{\theta}$ with $\tilde{\theta} = \tilde{\theta}(\theta, \phi)$ being the polar angle measured from the LOS, and $d\tilde{\Omega} = d\tilde{\varphi} d\tilde{\mu}$ is the solid angle. For an ultra-relativistic flow $\Gamma \gg 1$ for which $\delta_D \approx 2\Gamma/(1 + \tilde{\xi})$ with $\tilde{\xi} \equiv (\Gamma\tilde{\theta})^2$. The anisotropic comoving spectral luminosity for synchrotron emission can be expressed as (e.g., Rybicki & Lightman 1979)

$$L'_\nu = L'_\nu(R)(\sin \chi')^\epsilon = L'_\nu(R)[1 - (\hat{n}' \cdot \hat{B}')^2]^{\epsilon/2}, \quad (6)$$

where χ' is the angle between the direction of local magnetic field and that of the emitted photon in the comoving frame. Since synchrotron radiation is highly beamed in the forward direction of the electron's motion, χ' is also the pitch angle between the electron's velocity vector and the magnetic field. When the power-law electrons' energy distribution is independent of their pitch angles, $\epsilon = 1 + \alpha$ where $\alpha = -d \log F_\nu / d \log \nu$ is the spectral index (Laing 1980; Granot 2003).

The arrival time t of a photon originating at an angle $\tilde{\theta}$ and from a radius R is given by $t_z \equiv t/(1+z) = t_{\text{lab}} - R\tilde{\mu}/c$, where the lab-frame time for an ultra-relativistic thin-shell expanding with bulk LF $\Gamma(R) \propto R^{-m/2}$ is

$$t_{\text{lab}}(R) = \int_0^R \frac{dR'}{\beta(R')c} \approx \frac{R}{c} + \frac{R}{2(1+m)\Gamma^2 c} \quad (7)$$

for $m > -1$. Expressions for general $m \leq -1$ are straightforward. This yields the equal arrival time surface (EATS) for a given apparent time (e.g. Granot et al. 2008)

$$t_z(R, \tilde{\mu}) = \frac{R}{c} \left[1 - \tilde{\mu} + \frac{1}{2(1+m)\Gamma^2} \right] \approx \frac{R}{2\Gamma^2 c} \left(\tilde{\xi} + \frac{1}{1+m} \right), \quad (8)$$

where we made the approximation $\tilde{\mu} \approx 1 - \tilde{\theta}^2/2$ for $\tilde{\theta} \ll 1$ when $\Gamma \gg 1$ and where $\tilde{\xi} = (\Gamma\tilde{\theta})^2 = (\Gamma_0\tilde{\theta})^2 \hat{R}^{-m} = \tilde{\xi}_0 \hat{R}^{-m}$ with $\hat{R} \equiv R/R_0$. The arrival time of the first photons originating at radius R_0 and along the LOS with $\tilde{\mu} = 1$ ($\tilde{\xi} = 0$) is $t_{0,z} = R_0/2(1+m)\Gamma_0^2 c$ (where $t_z = 0$ corresponds to the arrival time of a hypothetical photon emitted at the central source together with the ejection of the expanding relativistic thin shell). Normalizing the apparent time by $t_{0,z}$ allows to express the EATS condition in a more convenient form

$$\tilde{t} \equiv \frac{t_z}{t_{0,z}} = \tilde{t}_R + \tilde{t}_\theta = \hat{R}^{1+m} + (1+m)\tilde{\xi}_0 \hat{R}, \quad (9)$$

where we identify the normalized radial and angular delay times as \tilde{t}_R and \tilde{t}_θ . Then, for a given apparent time the arriving photons originate from different angles on the outflow with $-1 \leq \tilde{\mu} \leq 1$ (as well as different $0 \leq \tilde{\varphi} \leq 2\pi$ but $\tilde{\varphi}$ does not affect the arrival time as long as the emitting shell is spherical). This corresponds to different limiting radii⁴ $\hat{R}_{\text{min}} \leq \hat{R} \leq \hat{R}_{\text{max}}$. The minimum radius is obtained for

⁴ The limiting radii obtained here are strictly valid for a spherical flow and not for a top-hat jet (§4.2) when $\theta_{\text{obs}} > \theta_j$ and when $\tilde{t}_{0-} < \tilde{t} < \tilde{t}_{f-}$ and $\tilde{t}_{0+} < \tilde{t} < \tilde{t}_{f+}$. In such cases, these limiting radii can be used when the angular dependence of the emissivity is taken into account, so that only emission from parts of the EATS that intersect the jet is included.

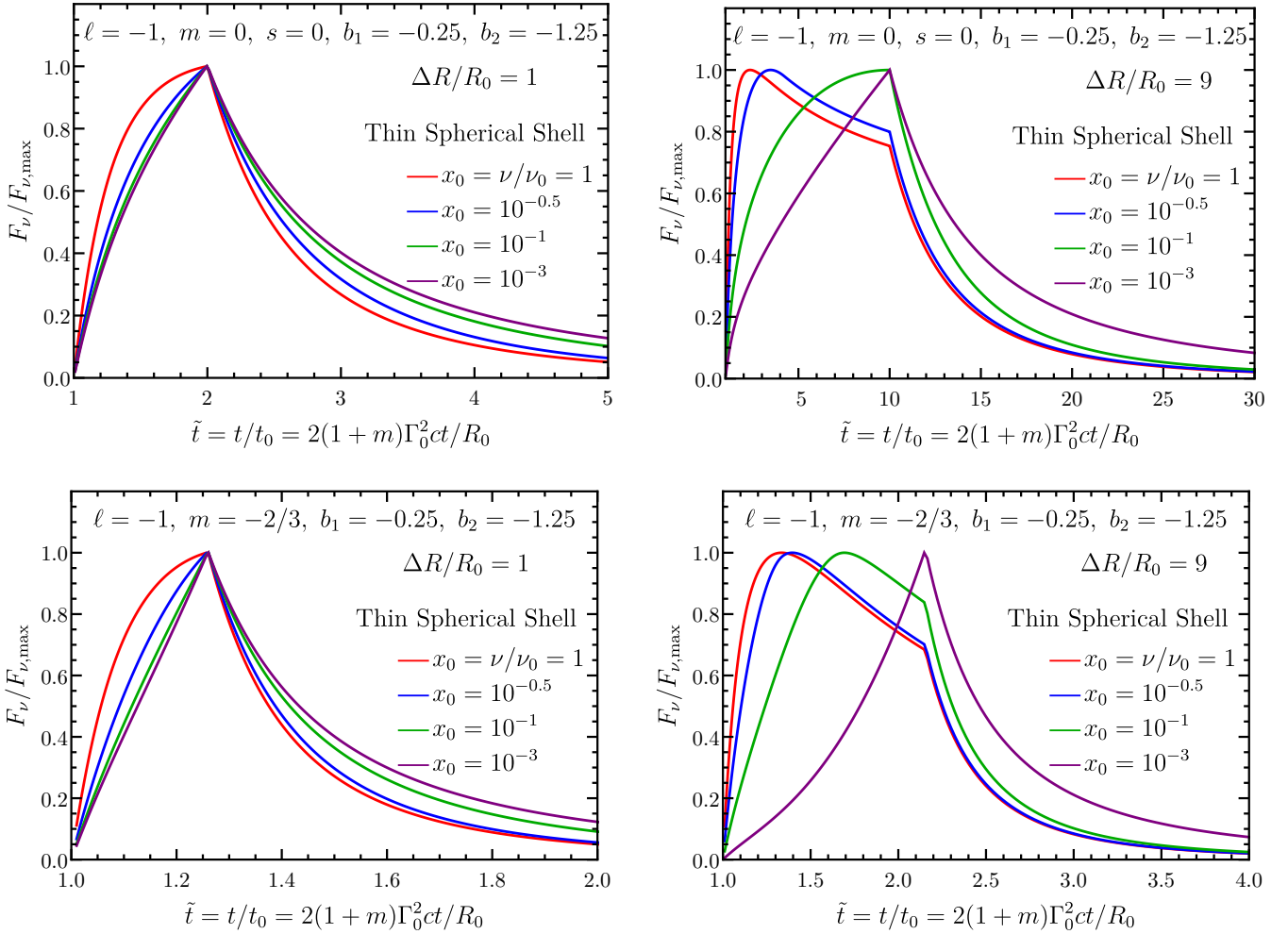


Figure 1. Pulse profiles for an ultrarelativistic thin spherical shell that is kinetic energy dominated (top; $a = 1$ and $d = -1$) or Poynting flux dominated (bottom; $a = 4/3$ and $d = -2$), shown as a function of the apparent time t normalized by the arrival time of the first photons emitted from radius R_0 along the LOS. The shell starts radiating at radius R_0 and continues to radiate over a radial distance of ΔR . The different curves show the trend at different observed frequencies $\nu = x_0 \nu_0$, where ν_0 is the spectral peak frequency of the photons that arrive at time t_0 .

$\tilde{\mu} = -1$ with $\hat{R}_{\min} = \max[1, \hat{R}_{\min}]$ where in general \hat{R}_{\min} is the root of the EATS equation

$$\tilde{t} = 4(1+m)\Gamma_0^2 \hat{R}_{\min} + \hat{R}_{\min}^{1+m}. \quad (10)$$

For an ultrarelativistic flow, with $\Gamma_0 \gg 1$, the above equation yields $\hat{R}_{\min} > 1$ only when $\tilde{t} \gg 1$, which is not relevant for our case here, and therefore, $\hat{R}_{\min} = 1$. The maximum radius is obtained for $\tilde{\mu} = 1$ with $\hat{R}_{\max} = \min[1 + \Delta R/R_0, \hat{R}_{\max}]$ with $\hat{R}_{\max} = \tilde{t}^{1/(1+m)}$. By using the EATS condition we can relate the integration over $\tilde{\mu}$ to that over R with $dR = |d\tilde{\mu}/dR|dR$ when calculating the flux density, where

$$R_0 \frac{d\tilde{\mu}}{dR} = \frac{d\tilde{\mu}}{d\hat{R}} = \frac{ct_z R_0}{R^2} \left[1 + \frac{m}{2(1+m)} \frac{R}{\Gamma^2 ct_z} \right] \quad (11)$$

$$= \frac{1}{2(1+m)\Gamma_0^2} \frac{\tilde{t}}{\hat{R}^2} \left[1 + \frac{m\hat{R}^{1+m}}{\tilde{t}} \right] \quad (12)$$

which yields

$$F_\nu(\tilde{t}) = \frac{(1+z)}{16\pi^2 d_L^2} \int_{\hat{R}_{\min}}^{\hat{R}_{\max}} d\hat{R} \left| \frac{d\tilde{\mu}}{d\hat{R}} \right| \delta_D^3 \int_0^{2\pi} d\tilde{\varphi} L'_\nu[\hat{R}, \theta(\hat{R}, \tilde{\varphi})], \quad (13)$$

where, for an ultrarelativistic flow, the Doppler factor can be ex-

pressed as

$$\delta_D \approx \frac{2\Gamma}{(1+\tilde{\xi})} = 2(1+m)\Gamma_0 \frac{\hat{R}^{-m/2}}{\hat{R}^{-(m+1)}\tilde{t}+m}. \quad (14)$$

The energy-dependent linear polarization can be expressed using the Stokes parameters, with $\Pi_\nu = \sqrt{Q_\nu^2 + U_\nu^2}/I_\nu$ where the specific intensity $I_\nu \propto F_\nu$ and ratio of the Stokes parameters (polarized intensities Q_ν and U_ν to the total intensity I_ν) can be obtained from (Gill et al. 2020a)

$$\left\{ \frac{Q_\nu(t_z)}{I_\nu(t_z)}, \frac{U_\nu(t_z)}{I_\nu(t_z)} \right\} = \frac{\int_{\hat{R}_{\min}}^{\hat{R}_{\max}} d\hat{R} \left| \frac{d\tilde{\mu}}{d\hat{R}} \right| \delta_D^3 L'_\nu(\hat{R}) \int_0^{2\pi} d\tilde{\varphi} \Lambda(\tilde{\xi}, \tilde{\varphi}) \Pi'}{\int_{\hat{R}_{\min}}^{\hat{R}_{\max}} d\hat{R} \left| \frac{d\tilde{\mu}}{d\hat{R}} \right| \delta_D^3 L'_\nu(\hat{R}) \int_0^{2\pi} d\tilde{\varphi} \Lambda(\tilde{\xi}, \tilde{\varphi})} \begin{Bmatrix} \cos(2\theta_p) \\ \sin(2\theta_p) \end{Bmatrix} \quad (15)$$

where $\Lambda(\tilde{\xi}, \tilde{\varphi}) = \langle [1 - (\hat{n}' \cdot \hat{B}')^2]^{\epsilon/2} \rangle$ represents the factor relating to the pitch angle of electrons averaged over the local probability distribution of the comoving magnetic field \hat{B}' , and Π' is the local (and not averaged over the whole observed region of the emitting shell) degree of polarization. Expressions for $\Lambda(\tilde{\xi}, \tilde{\varphi})$, θ_p , and Π' for

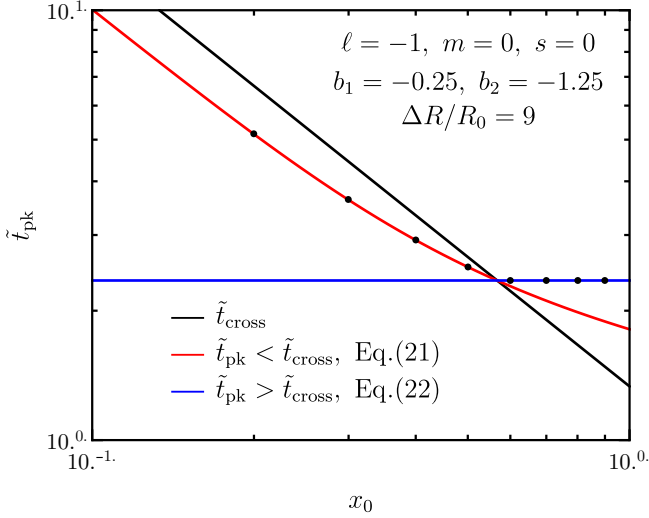


Figure 2. The peak time of pulses from the full numerical solution (Eq. 13) with different x_0 are shown using black dots. These are compared with analytic solutions obtained from $dF_v/d\tilde{t} = 0$, where approximate scaling of the flux $F_v(\tilde{t})$ is given in Eq. (16). It's clear that the pulse peak times don't exactly follow the crossing time (\tilde{t}_{cross}) of the spectral break energy that can only be used as a zeroth-order approximation.

different magnetic field configurations and assuming an ultrarelativistic uniform flow were first derived in Granot (2003); Granot & Königl (2003); Lyutikov et al. (2003); Granot & Taylor (2005) and are summarized in Toma et al. (2009); Gill et al. (2020a). For an axisymmetric flow, $U_v = 0$ due to symmetry, and the instantaneous polarization is given by $\Pi_v = Q_v/I_v$. For an axisymmetric flow, the net polarization can only be aligned with two direction, either along the line connecting the LOS and the jet symmetry axis ($\Pi < 0$) on the plane of the sky or transverse to it ($\Pi > 0$).

We consider different magnetic field configurations here, including tangled fields (B_\perp) constrained to be in the plane transverse to the local velocity vector, which we take to be in the radial direction, fields (B_\parallel) that are ordered along the direction of the local velocity vector, ordered fields (B_{ord}) in the plane of the ejecta with angular coherence scales $\theta_B \gtrsim 1/\Gamma$, and a globally ordered toroidal field (B_{tor}) that is axisymmetric around the jet symmetry axis and is ordered in the transverse direction.

4.1 Polarization from a thin spherical shell

We first consider the simplest scenario of an ultrarelativistic thin spherical shell, where the emission region is pervaded by a locally ordered B-field (B_{ord}) that lies in the plane transverse to the local fluid velocity, $\vec{\beta} = (v/c)\hat{R}$ with v being the fluid velocity, which we take to be in the radial direction with unit vector \hat{R} . This case is both instructive and relevant when the jet has sharp edges, with half-opening angle θ_j , and the observer is on-beam (see Table 1 and §4.2 for definition), with viewing angle $\theta_{\text{obs}} \lesssim \theta_j - 1/\Gamma$, so that the emission is indistinguishable from that arising from a spherical flow at early times when the observer is unaware of the jet's edge. The field is ordered with an angular coherence length scale $\theta_B \gtrsim 1/\Gamma$, where $\tilde{\theta} = 1/\Gamma$ is the angular size of the beaming cone.

The approximate scaling of flux density with \tilde{t} can be derived from

Eq. (13) to obtain

$$F_v(\tilde{t}) \propto \tilde{t} \hat{R}^{a-1} \left(1 + \frac{m \hat{R}^{1+m}}{\tilde{t}} \right) \left(\frac{\hat{R}^{-m/2}}{\hat{R}^{-(m+1)\tilde{t}} + m} \right)^3 S(x) \Big|_{\hat{R}_{\text{min}}}^{\hat{R}_{\text{max}}}, \quad (16)$$

where this expression is evaluated at the two limiting radii, and where $S(x) \propto x^{b_1} \exp[-(1+b_1)x]$ for $x \leq x_b$ and $S(x) \propto x^{b_2}$ for $x > x_b$ with

$$x = \frac{2\Gamma_0}{\delta_D} \frac{x_0}{\hat{R}^d} = \frac{x_0}{1+m} \frac{\hat{R}^{-(m+1)\tilde{t}} + m}{\hat{R}^{(2d-m)/2}}. \quad (17)$$

There are two important timescales at which the behavior of the flux density and polarization changes, namely (i) the crossing time, \tilde{t}_{cross} , of the spectral break frequency (x_b) across a given observed frequency (x) for the emission from the LOS, after which point the observer only samples the spectrum above the spectral break frequency, which for the Band-function is a strict power-law, and (ii) the timescale $\tilde{t}_f = \hat{R}_f^{1+m}$ that corresponds to the arrival of the last photons emitted along the LOS from radius R_f at which emission is suddenly switched off. Exact expressions for the flux density for different temporal power-law segments are derived in Genet & Granot (2009).

When the spectral break crossing occurs at $\tilde{t} < \tilde{t}_f$, the emission is dominated by that along the LOS. In this case, the time of the spectral break crossing can be approximately obtained from Eq. (17) with $\tilde{t} = \tilde{t}_R = \hat{R}^{1+m}$, the radial delay time for the arrival of the first photons along the LOS from any radius, so that

$$x_b = x = x_0 \tilde{t}^{(m-2d)/2(1+m)} \Rightarrow \tilde{t}_{\text{cross}} \approx \left(\frac{x_b}{x_0} \right)^{2(1+m)/(m-2d)}, \quad x_0 < 1. \quad (18)$$

The crossing time derived above is only approximate and not exact since the observer receives emission from different radii. Although the dominant contribution does come from emission along the LOS, the contribution from smaller radii has a small but non-negligible effect on \tilde{t}_{cross} . Since for the outflow dynamics considered here $m > -1$, and if $d \leq m/2$ as well, which is true for the two types of outflows considered in this work, then the crossing time increases with decreasing energy x_0 . In that case, for $\tilde{t} > \tilde{t}_{\text{cross}}$ the pulse profile for a given $x_0 = x_{0,a}$ should have an exactly similar trend with \tilde{t} as for pulses with $x_0 = x_{0,b} > x_{0,a}$, if all else remains unchanged. Furthermore, since the degree of polarization depends on the spectral index, the polarization for $x_0 = x_{0,a}$ at any given $\tilde{t} > \tilde{t}_{\text{cross}}$ should be exactly the same as that for $x_0 = x_{0,b} > x_{0,a}$. In the case of a KED flow, with $m = 0$ and $d = -1$, we get

$$\tilde{t}_{\text{cross}} \approx \frac{x_b}{x_0}. \quad (19)$$

When the spectral break crossing occurs at $\tilde{t} > \tilde{t}_f$, there is no longer emission arriving along the LOS. Instead, the flux is dominated by emission from $\hat{R} = \hat{R}_f$ but from angles away from the LOS, with $\tilde{\theta} \geq \tilde{\theta}_f > 0$ where $\tilde{\theta}_f = \Gamma_0^{-1}[(\tilde{t} - \tilde{t}_f)/(1+m)\hat{R}_f]^{1/2}$ (for $\tilde{\theta}_f \ll 1$). In this case, \tilde{t}_{cross} can be approximated using Eq. (17), now evaluated at $\hat{R} = \hat{R}_f$ for $x = x_b$, which yields

$$\tilde{t}_{\text{cross}} \approx \left[(1+m) \left(\frac{x_b}{x_0} \right) \hat{R}_f^{(2d-m)/2} - m \right] \hat{R}_f^{1+m}, \quad x_0 < 1. \quad (20)$$

Interestingly, for the special case of a KED flow with $m = 0$ and $d = -1$, we recover Eq. (19).

In Fig. 1, we show the pulse profiles for a KED (top row) and a PFD (bottom row) flows with $\Delta R/R_0 = \{1, 9\}$ for different $x_0 = v/v_0$. Similar results have also been obtained in Genet & Granot (2009); Uhm & Zhang (2015, 2016). The pulse profiles are shown using normalized flux $F_v/F_{v,\text{max}}$ as a function of \tilde{t} , where $F_{v,\text{max}}$ is the

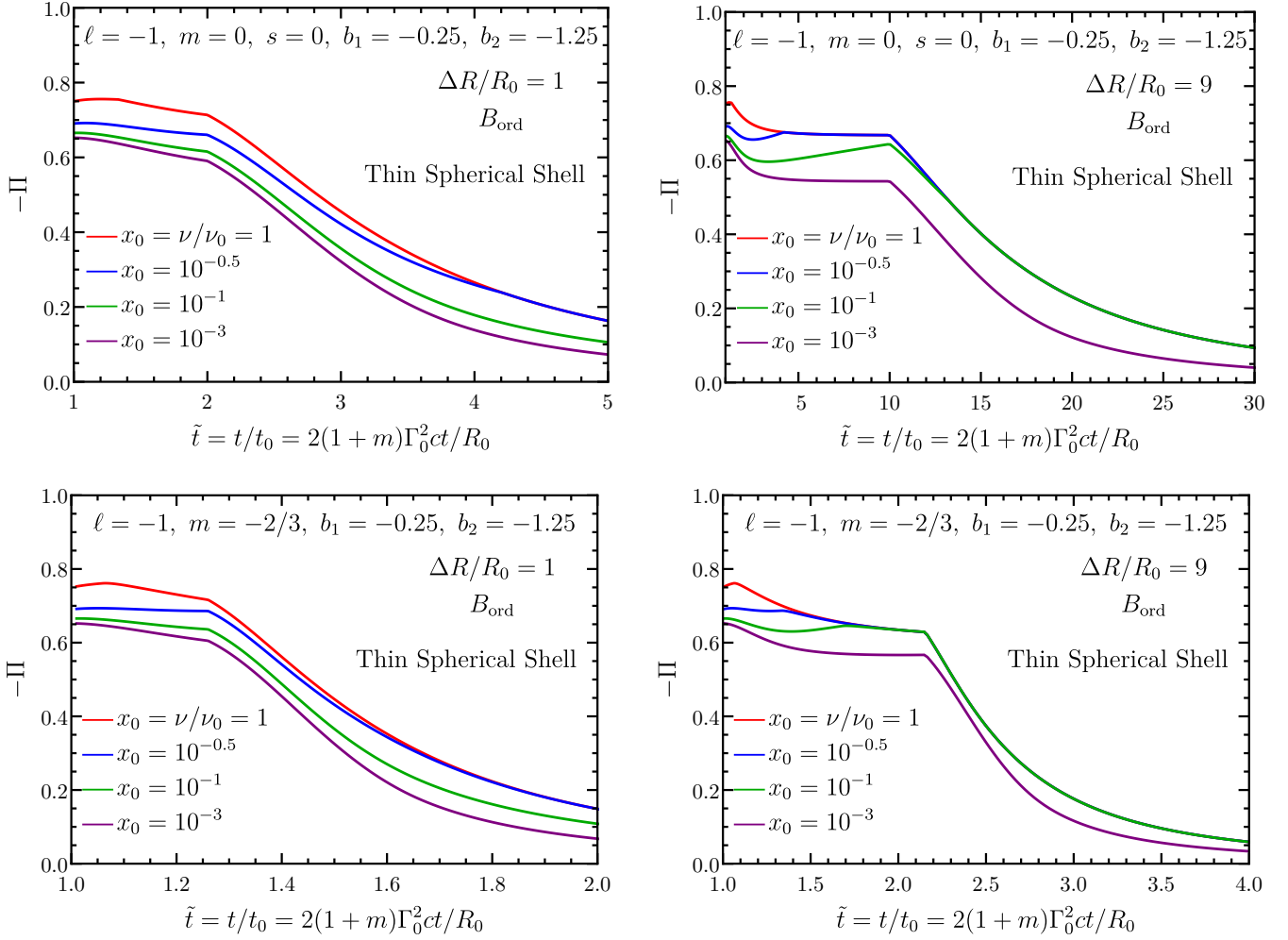


Figure 3. Temporal evolution of polarization over a pulse shown for the same flow dynamics as in Fig. 1, with KED (top; $a = 1$ and $d = -1$) and PFD (bottom; $a = 4/3$ and $d = -2$) flows. The magnetic field is assumed to be ordered with angular coherence length, $\theta_B \gtrsim 1/\Gamma$, larger than the observed region of the flow. See Table 1 and caption of Fig. 1 for definition of various symbols.

maximum flux density. For $\Delta R/R_0 = 1$, $F_{v,\max} = F_v(\tilde{t}_f)$ where $\tilde{t}_f = \hat{R}_f^{1+m} = (1 + \Delta R/R_0)^{1+m}$ gives the normalized arrival time of the last photon emitted along the LOS when the emission is switched off at $R_f = R_0 + \Delta R$. Then, for $1 \leq \tilde{t} \leq \tilde{t}_f$, the flux rises to its peak and decays abruptly at $\tilde{t} > \tilde{t}_f$ after which point high latitude emission starts to dominate. All the curves show temporal slopes that are dissimilar from each other, and only at late times when $\tilde{t} > \tilde{t}_{\text{cross}}(x_0)$ the temporal slopes of curves with $x_0 < 1$ match with that of $x_0 = 1$. One of the main differences between the $m = 0$ (top-left) and $m = -2/3$ (bottom-left) case is that there is a linear relation between $\tilde{t}_f = \tilde{t}_f - 1$ and $\Delta R/R_0$ which is not true for an accelerating ($m < 0$) flow. The pulse profiles do show subtle differences between the two cases, e.g. when comparing the $x_0 = 10^{-3}$ curves when $\Delta R/R_0 = 1$, the $m = 0$ case shows a curved pulse profile up to the peak whereas the $m = -2/3$ case shows a much more linear rise to the peak. These differences are even more pronounced when $\Delta R/R_0 = 9$.

For the $\Delta R/R_0 = 9$ ($\hat{R}_f = 10$) case (right column of Fig. 1), the pulse profiles show a peak at $\tilde{t}_{\text{pk}} < \tilde{t}_f$ instead. The reason for this behavior is the passage of the spectral peak across the observed frequency which, despite the rise of the peak spectral power, $L'_{\nu',\max} \propto R^{-(\ell+s)}$, with radius, causes the observed flux density to

decline. Such a peak occurs at $\tilde{t}_{\text{pk}} < \tilde{t}_f$ for $x_0 \gtrsim x_b \hat{R}_f^{(2d-m)/2}$ i.e. $x_0 \gtrsim 0.133$ for a KED flow and $x_0 \gtrsim 0.029$ for a PFD flow for our parameter values. After the pulse peak, it can be seen that all curves show the same temporal slope, except the green and purple curves for $m = 0$ and only the purple curve for $m = -2/3$ for which $\tilde{t}_{\text{cross}} > \tilde{t}_f$. Since the Band spectrum is smoothly broken at the spectral peak, rather than having a sharp break, the pulse peak can lie both before or after \tilde{t}_{cross} due to the curvature. The scaling of the flux density in the two relevant time segments, $\tilde{t} < \tilde{t}_{\text{cross}} < \tilde{t}_f$ and $\tilde{t}_{\text{cross}} < \tilde{t} < \tilde{t}_f$ can be obtained from Eq. (16). The peak of the pulse is obtained from $dF_v/d\tilde{t} = 0$, which for a KED flow ($m = 0, a = 1, d = -1$) yields the equations

$$(\tilde{t}_{\text{pk}}^4 - \tilde{t}_{\text{pk}})x_0 - \tilde{t}_{\text{pk}}^3 = \frac{2 - b_1}{1 + b_1}, \quad \tilde{t}_{\text{pk}} < \tilde{t}_{\text{cross}} < \tilde{t}_f \quad (21)$$

$$\tilde{t}_{\text{pk}} = \left(\frac{b_2 - 2}{b_2 + 1} \right)^{1/3}, \quad \tilde{t}_{\text{cross}} < \tilde{t}_{\text{pk}} < \tilde{t}_f. \quad (22)$$

Here Eq. (21) is implicit and the peak time is obtained by root finding. We show both solutions in Fig. 2 and compare them with the peak times of pulses with different x_0 . The solution from Eq. (21) asymptotically becomes parallel to $\tilde{t}_{\text{cross}}(x_0)$ but scaled down in mag-

nitute. This scale factor can be derived by looking at the $x_0 \ll 1$ and $\tilde{t}_{\text{pk}} \gg 1$ limit of Eq. (21) that yields $\tilde{t}_{\text{pk}} = x_0^{-1}$, and therefore the scale factor is $\tilde{t}_{\text{cross}}/\tilde{t}_{\text{pk}} = x_b$.

The temporal evolution of polarization is shown in Fig. 3 for different values of x_0 and $\Delta R/R_0$, and it is broadly similar for the two different outflows. Initially, at $\tilde{t} \approx 1$, since the emission is dominated by photons along the LOS, the polarization shows the maximum degree ($\Pi = \Pi_{\text{max}}$) for the local spectral index sampled for a given x_0 . Due to the curvature of the spectrum near the spectral peak, the local spectral index varies as x_0 is decreased until the asymptotic index is reached. At $\tilde{t} > 1$, the observer sees photons emerging from within the entire beaming cone which causes the polarization to decline and saturate due to partial cancellation. At $\tilde{t} > \tilde{t}_f$ high latitude emission dominates and the polarization shows a steep decline. For all the cases shown, the polarization curves corresponding to $x_0 < 1$ merge with that for $x_0 = 1$ at $\tilde{t} \approx \tilde{t}_{\text{cross}}(x_0)$ due to crossing of the break frequency across the observed frequency.

Here we have only considered a locally ordered magnetic field configuration since it naturally breaks the symmetry in an axisymmetric flow and yields non-vanishing polarization. Similar results can be obtained for a globally ordered toroidal field, B_{tor} . On the other hand, a uniform spherical flow would always yield zero net polarization for the B_{\perp} and B_{\parallel} fields due to complete cancellation of polarization after averaging over the GRB image over the plane of the sky. Therefore, an inhomogeneous flow or jet geometry with sharp/smooth edges, as treated in the next section, is needed to break the symmetry.

4.2 Polarization from a top-hat jet

For a top-hat jet the emissivity vanishes for $\theta > \theta_j$, where θ_j is the jet half-opening angle, such that $L'_{\nu} \rightarrow L'_{\nu} H(\xi_{0,j} - \xi_0)$ where $H(x)$ is the Heaviside function, $\xi_{0,j} = (\Gamma_0 \theta_j)^2$, and $\xi_0 = (\Gamma_0 \theta)^2$. The polar angle θ can be related to $\tilde{\theta}$ and $\tilde{\varphi}$ using the general relation

$$\cos \theta = \mu = \mu_{\text{obs}} \tilde{\mu} - \cos \tilde{\varphi} \sqrt{(1 - \tilde{\mu}^2)(1 - \mu_{\text{obs}}^2)}, \quad (23)$$

with $\tilde{\mu} = \cos \tilde{\theta}$ and $\mu_{\text{obs}} = \cos \theta_{\text{obs}}$. For an ultra-relativistic flow, this relation simplifies to

$$\xi_0 = \tilde{\xi}_0 + q^2 \xi_{0,j} + 2q \cos \tilde{\varphi} \sqrt{\tilde{\xi}_0 \xi_{0,j}}, \quad (24)$$

where we define $q \equiv \theta_{\text{obs}}/\theta_j$ and where the temporal and radial dependence of $\tilde{\xi}_0 = (\Gamma_0 \tilde{\theta})^2 = (\tilde{t} \hat{R}^{-1} - \hat{R}^m)/(1+m)$ is obtained from the EATS condition.

The top-hat jet case presents significant differences from the spherical flow geometry for different viewing angles q . Therefore, we briefly establish the appropriate terminology here. The observer is said to be ‘on-beam’ when emission is received within the $1/\Gamma$ beaming cone of the emitting material. For a spherical shell this is always the case and the observer is on-beam regardless of the viewing angle. In the case of a top-hat jet, the observer receives on-beam emission only when $q \lesssim 1 + \xi_j^{-1/2} \Leftrightarrow \theta_{\text{obs}} \lesssim \theta_j + 1/\Gamma$. Otherwise, the observer is ‘off-beam’ when the emission is received from outside of the $1/\Gamma$ beaming cone of the emitting material. This situation arises when $q > 1 + \xi_j^{-1/2} \Leftrightarrow \theta_{\text{obs}} > \theta_j + 1/\Gamma$. For an on-beam observer the pulse profile should be similar to that obtained for a spherical flow. More often the terms ‘on-axis’ and ‘off-axis’ are used in the literature when discussing top-hat jets, where these are synonymous with on-beam and off-beam cases. Care should be taken when describing structured jets, in which both the emissivity and bulk- Γ decline with increasing θ outside of a quasi-uniform core. In this case, the observer can be off-axis (now with viewing angle outside of the core)

and still receive on-axis or on-beam emission since there’s always material that could emit along the LOS. If the gradient in emissivity and/or bulk- Γ is sufficiently steep, the emission is dominated by brighter regions at angles $\theta < \theta_{\text{obs}}$, in which case the observer would only receive off-beam emission.

In the case of a top-hat jet, there are several critical timescales at which both the pulse profile as well as the polarization curve undergo a change, regardless of the fact that the received emission is on-beam or off-beam. These timescales are demonstrated using two dimensional (2D) cross-sections out of the 3D EATSs in Fig. 4 for a coasting jet with $\Gamma = \Gamma_0$. The top-panel shows the EATSs for an on-beam observer. Similar to the case of a spherical flow discussed earlier, the observer starts receiving emission along the LOS at $\tilde{t} = 1$ when the thin shell is at $\hat{R} \equiv R/R_0 = 1$. Emission along the LOS terminates at $\tilde{t} = \tilde{t}_f$ when the shell reaches $\hat{R} = \hat{R}_f$. Next, at $\tilde{t} > \tilde{t}_f$, the observer continues to receive emission from increasingly larger $\tilde{\theta} > 0$ where the emission becomes dominated by that arising from higher latitudes, i.e. when $\tilde{\theta} > 1/\Gamma$. Any emission arising from $\tilde{\theta} > 0$ suffers an angular delay in addition to the radial one, and the arrival time of photons is readily obtained from the EATS condition in Eq. (9) that yields

$$\tilde{t}(\tilde{\theta}) = \hat{R}^{1+m} \left[1 + (1+m) \left(\frac{\tilde{\theta}}{\theta_j} \right)^2 \frac{\xi_{0,j}}{\hat{R}^m} \right], \quad (25)$$

where we made use of the fact that $\tilde{\xi}_0 = (\Gamma_0 \tilde{\theta})^2 = (\tilde{\theta}/\theta_j)^2 \xi_{0,j}$. The radial and angular times are equal when

$$\tilde{\theta} = \frac{\hat{R}^{m/2}}{(1+m)^{1/2}} \frac{1}{\Gamma_0}, \quad (26)$$

which for $m = 0$ yields the well known result, $\tilde{\theta} = 1/\Gamma_0$. A critical change both in the pulse profile and polarization curve occurs whenever the observer becomes aware of the edge of the jet at both $R = R_0$ and $R = R_f$. The arrival time of photons emitted at any \hat{R} from the edges of the jet, corresponding to the condition $\tilde{\theta}/\theta_j = 1 \pm q$, is given by

$$\tilde{t}_{\pm} = \hat{R}^{1+m} [1 + (1+m)(1 \pm q)^2 \hat{R}^{-m} \xi_{0,j}], \quad (27)$$

where the negative and positive solutions correspond to the nearer and farther edges from the LOS, respectively. For a coasting flow, the case shown in Fig. 4, $m = 0$ for which we get

$$\tilde{t}_{\pm} = \hat{R} [1 + (1 \pm q)^2 \xi_{0,j}] \quad (m = 0). \quad (28)$$

From here we define the following critical timescales

$$\begin{aligned} \tilde{t}_{0-} &\equiv \tilde{t}_-(\hat{R} = 1) = 1 + (1 - q)^2 \xi_{0,j}, \\ \tilde{t}_{f-} &\equiv \tilde{t}_-(\hat{R} = \hat{R}_f) = \hat{R}_f [1 + (1 - q)^2 \xi_{0,j}], \\ \tilde{t}_{0+} &\equiv \tilde{t}_+(\hat{R} = 1) = 1 + (1 + q)^2 \xi_{0,j}, \\ \tilde{t}_{f+} &\equiv \tilde{t}_+(\hat{R} = \hat{R}_f) = \hat{R}_f [1 + (1 + q)^2 \xi_{0,j}]. \end{aligned} \quad (29)$$

For a more general m we have

$$\begin{aligned} \tilde{t}_{0\pm} &= 1 + (1+m)(1 \pm q)^2 \xi_{0,j}, \\ \tilde{t}_{f\pm} &= \tilde{t}_f + (1+m)(1 \pm q)^2 \xi_{0,j} \hat{R}_f. \end{aligned} \quad (30)$$

Notice, when $q = 0$ the observer receives photons from both edges of the jet at the same time, such that $\tilde{t}_{-} = \tilde{t}_{+}$. For $\tilde{t} > \tilde{t}_{f+}$ the flux goes to zero since this marks the arrival time of the last photons from the jet.

The bottom panel of Fig. 4 depicts the situation for an off-beam observer with $q \gtrsim 1 + \xi_j^{-1/2}$, which implies that there is no on-beam emission and the observer only receives high-latitude (off-beam) emission. Therefore, the first photons arrive from the nearer edge

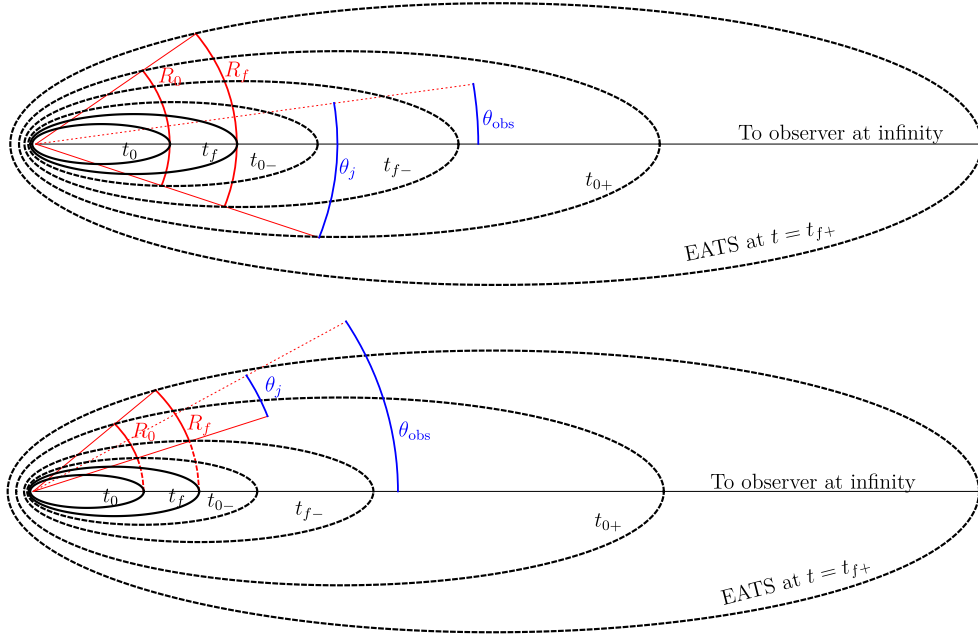


Figure 4. Two-dimensional cross-sections out of three-dimensional equal arrival time surfaces (EATs) for an observer (with $\theta_{\text{obs}} > 0$) receiving on-beam (top; $\theta_{\text{obs}} < \theta_j + 1/\Gamma$) and off-beam (bottom; $\theta_{\text{obs}} > \theta_j + 1/\Gamma$) emission from a top-hat jet coasting at a constant Γ ($m = 0$). The spherical thin shell with sharp edges (at $\theta = \theta_j$; all angles are measured from the jet symmetry axis (red dotted line)) starts to radiate at $R = R_0$ and stops at $R = R_f$. **Top:** The on-beam emission arrival time of first photons emitted at $R = R_0$ along the LOS is $t = t_0$, while the same for photons emitted at $R = R_f$ is $t = t_f$. At $t > t_f$ high latitude emission (dashed EATS) starts to dominate the observed flux and the photon arrival time is further delayed by the angular delay time in addition to the radial delay. At $t = t_{0-}$ (see Eq. 29), high-latitude emission arrives from the nearer edge of the jet when the shell is at $R = R_0$. Subsequently, high latitude emission arrives from the nearer edge at $R = R_f$ at $t = t_{f-}$, then from the farther edges at $R = R_0$ at $t = t_{0+}$ and from $R = R_f$ at $t = t_{f+}$. While the relative orderings $t_0 \leq t_{0-} \leq t_{0+}$, $t_0 < t_f \leq t_{f-} \leq t_{f+}$ (the left and right equalities holding for $\theta_{\text{obs}} = \theta_j$ and $\theta_{\text{obs}} = 0$, respectively), $t_{0-} < t_{f-}$ and $t_{0+} < t_{f+}$ always hold, the relative orderings of $t_f, t_{0-}, t_{0+}, t_{f-}$ can be different from the particular case shown here, i.e. (1a) $t_0 < t_f < t_{0-} < t_{f-} < t_{0+} < t_{f+}$. Other possible relative time orderings for different R_f and q are: (1b) $t_0 < t_f < t_{0-} < t_{0+} < t_{f-} < t_{f+}$, (2a) $t_0 < t_{0-} < t_f < t_{f-} < t_{0+} < t_{f+}$, (2b) $t_0 < t_{0-} < t_f < t_{0+} < t_{f-} < t_{f+}$, and (2c) $t_0 < t_{0-} < t_{0+} < t_f < t_{f-} < t_{f+}$. For on-beam emission, all of these angular timescales are particularly important for the calculation of polarization (see Fig. 5). **Bottom:** For off-beam emission, the arrival time of first photons from radius R_0 is determined by both the radial and angular delay time so that first photons arrive at $t = t_{0-}$ and the same from radius R_f is given by $t = t_{f-}$. The arrival time of last photons, corresponding to the farther edge of the jet, from $R = R_0$ is given by $t = t_{0+}$ and the same from $R = R_f$ is given by $t = t_{f+}$.

of the jet at $\tilde{t} = \tilde{t}_{0-}$ and the last photons emitted at $R = R_0$ arrive from the farther edge at $\tilde{t} = \tilde{t}_{0+}$. Likewise, photons from the nearer and farther edges arrive at $\tilde{t} = \tilde{t}_{f-}$ and $\tilde{t} = \tilde{t}_{f+}$, respectively, when the shell is at $R = R_f$.

The timescales at which the observer becomes aware of the edge of the jet and starts noticing a deficit in flux has important implications for the polarization. We demonstrate this schematically for two magnetic field configurations, B_\perp and B_{tor} , in Fig. 5, again for a uniform coasting flow ($m = 0$). The expectation for the change in polarization across these timescales is different for the two field configurations. The top panel of the figure shows the polarization map for the B_\perp field on the surface of the outflow for an on-beam observer. The blue and green shaded regions show the area of the flow that are predominantly polarized in the direction along the line connecting the LOS and the jet symmetry axis ($\Pi < 0$) and that are polarized in the transverse direction ($\Pi > 0$), respectively. Due to the inherent symmetry around the LOS $\Pi = 0$ at all times $\tilde{t} \leq \tilde{t}_{0-}$. As soon as the edge of the jet becomes apparent the missing flux from $R = R_0$ breaks this symmetry which should yield a net non-zero polarization at $\tilde{t} > \tilde{t}_{0-}$. Initially, the green shaded regions dominate that yield $\Pi > 0$, and as the observer receives emission from larger angles the blue shaded regions start to dominate. This produces $\Pi < 0$ and, as a result, the PA changes by 90° . The observer receives the last photon from the jet at $\tilde{t} = \tilde{t}_{f+}$, after which time the flux goes

to zero and naturally so does the polarization. When the observer is off-beam symmetry is broken from the beginning of the pulse as the observer receives the first photons from the nearer edge of the jet. In this case, the polarization is expected to be maximal at the start of the pulse at $\tilde{t} = \tilde{t}_{0-}$ (with $\Pi = \Pi_{\text{max}}$ for B_{tor} or B_\parallel but $\Pi < \Pi_{\text{max}}$ for B_\perp , as the flux comes from a single point of the jet without any canceling between different parts) followed by a decline as increasingly larger area of the outflow comes into view. In addition, since in this case only the blue shaded region remains dominant, the PA remains constant with $\Pi < 0$ at all times.

The bottom panel of Fig. 5 shows the polarization map for the B_{tor} configuration⁵, again for an on-beam (left-panel) and off-beam (right-panel) observer. However, in contrast to the B_\perp or even B_\parallel case, since the field is ordered the polarization is maximal right from the reception of the first photon. As was seen in the locally ordered

⁵ In Granot (2003) θ_p is measured from the direction transverse to the line connecting the jet symmetry axis and the LOS, the same is adopted in the present work, however, in Granot & Taylor (2005) θ_p is measured from the line connecting the jet axis and LOS instead. The former parameterization would yield $\Pi < 0$ when integrated over the pulse for the B_{tor} case, leading to an opposite sign from what's shown in Gill & Granot (2020) who adopted the latter parameterization for θ_p only for the B_{tor} case.

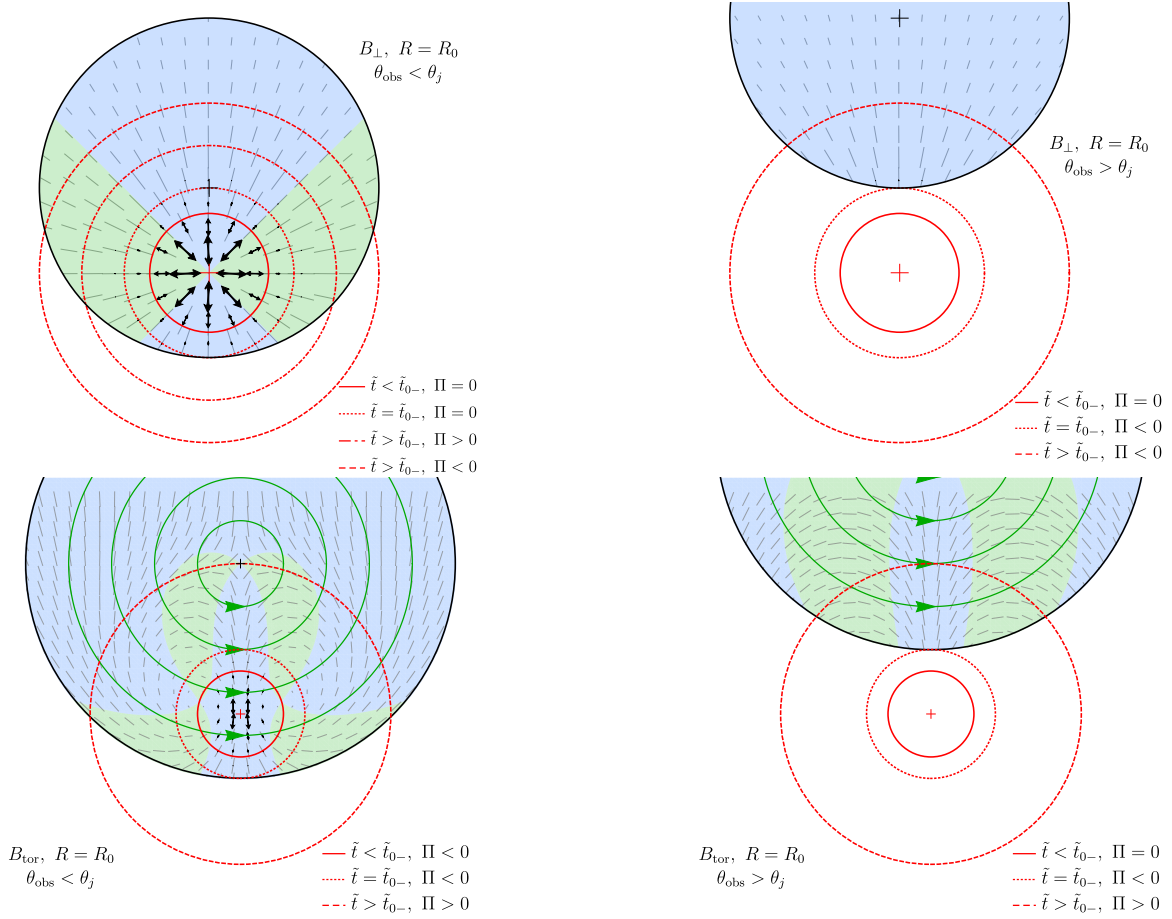


Figure 5. Schematics showing the observed area on the plane of the sky of a top-hat jet coasting at constant bulk Γ and its implications for the temporal evolution of polarization. The aperture of the jet is indicated by a black circle with black plus symbol denoting the jet symmetry axis. The aperture of the beaming cone around the observer's LOS, shown with a red plus symbol, with angular extent $\Gamma\tilde{\theta} = 1$ is shown with a solid red circle. The cross-section of the EATS that contributes to the high-latitude emission is shown with a dotted red circle. **Top:** The polarization map for the B_{\perp} field configuration for a LOS with $q = 0.5$ (left) and $q = 1.5$ (right) is shown over the entire aperture of the flow with gray line segments. The size of the black arrows in the beaming cone reflects the polarized intensity, whereas the gray line segments are normalized by $\delta^{3+\beta}$, with β being the spectral index, for clarity. The blue shaded regions contribute a net polarization along the line on the plane of the sky that connects the jet symmetry axis and the LOS ($dQ_v \propto \cos(2\theta_p) < 0$), whereas the green shaded regions contribute a net polarization in the transverse direction ($dQ_v \propto \cos(2\theta_p) > 0$), which is also the direction from which θ_p is measured. The predominance of these regions decides the orientation of the net polarization which switches sign going from initially green dominated to blue dominated. In the right panel, the PA remains constant. For the B_{\perp} (and also for B_{\parallel}) configuration, the polarization starts to grow above zero at $\tilde{t} \geq \tilde{t}_{0-}$ due to missing flux that breaks the symmetry. This polarization ‘break’ can be used to constrain the jet half-opening angle. For $q > 1 + \xi_j^{-1/2}$, the emission starts maximally polarized at $\tilde{t} = \tilde{t}_{0-}$ after which time the polarization starts to decline. **Bottom:** Polarization map for the B_{tor} field configuration with $q = 0.7$ (left) and $q = 1.3$ (right) is shown at three different times where the polarization undergoes a 90° change at $\tilde{t} > \tilde{t}_{0-}$ at which point the green shaded region dominates over the blue. Another 90° change in PA occurs at late times when the blue region becomes dominant. The field lines, shown in green, are symmetric around the jet axis. The emission is maximally polarized at $\tilde{t} = 1$ and shows a sharp decline at $\tilde{t} > \tilde{t}_f$ at which point high-latitude emission becomes dominant.

field case, the polarization would start to decline rapidly when high-latitude emission becomes dominant. As discussed below, the PA changes by 90° twice in this case depending on which (blue/green) region dominates at any given time.

While the polarization maps provide a qualitative understanding of how the polarization should evolve over the pulse, a more quantitative picture is shown in Fig. 6 where we show the polarization curves for the different field configurations and viewing angles⁶.

⁶ To calculate the pulse profile and polarization we use the general expression valid for a spherical shell (given by Eq. 15), but use the Heaviside function to suppress the emissivity for $\xi_0 > \xi_{0,j}$. While this technique is more suitable for a structured flow, or a smooth top-hat jet as treated in later sec-

In the figure the critical timescales are presented to allow comparison with the polarization maps. Two cases are highlighted, one with $\xi_j = 10^2$ and $\Delta R/R_0 = 1$ (top panel) and the other with $\xi_j = 10$ and $\Delta R/R_0 = 9$ (bottom panel), where they have interesting differences. In both the left and right panels, corresponding to an on-beam and off-beam observer, respectively, the polarization behavior matches the expectation from the polarization maps. In the top panel, the polarization curve for the B_{tor} case undergoes a 90° change in PA twice

tions, it may be slightly computationally expensive for a top-hat jet due to the sharp edge in emissivity. More suitable expressions for calculating the lightcurve and polarization for a top-hat jet are given in Ghisellini & Lazzati (1999) for $q < 1$ and in Granot (2003) for a general q .

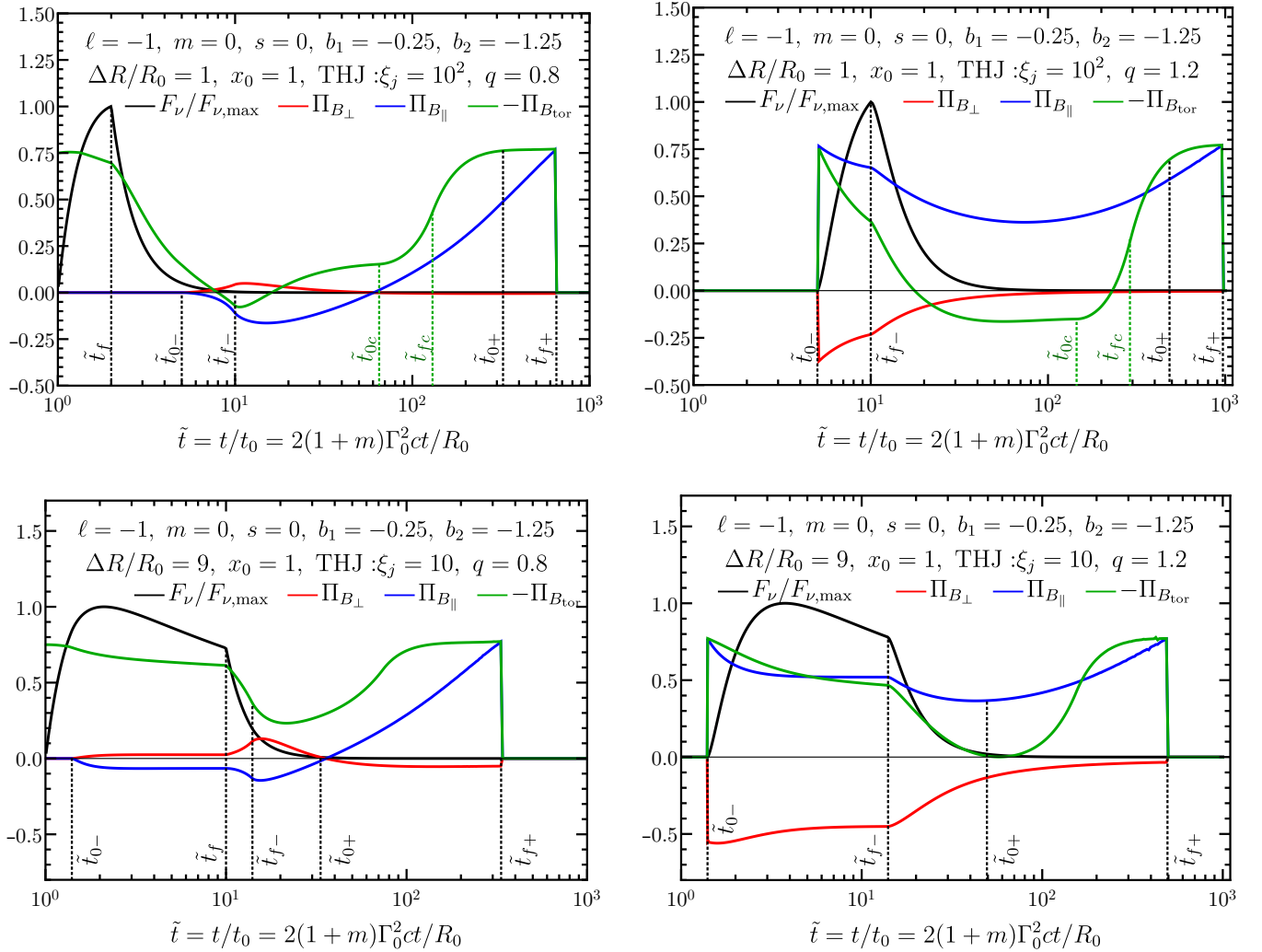


Figure 6. Pulse profile and polarization temporal evolution over a single pulse shown for different magnetic field configurations. The outflow dynamics are that of a KED flow with a top-hat jet geometry with $\xi_j = (\Gamma\theta_j)^2 = 100$ and $\Delta R/R_0 = 1$ (top) and $\xi_j = (\Gamma\theta_j)^2 = 10$ and $\Delta R/R_0 = 9$ (bottom), both shown for $q = \theta_{\text{obs}}/\theta_j = 0.8$ (left; on-beam emission) and $q = 1.2$ (right; off-beam emission). The critical timescales corresponding to the EATS shown in Fig. 4 are shown with vertical dotted lines. The angular timescales \tilde{t}_{0c} and $\tilde{t}_{fc} = \tilde{R}_f \tilde{t}_{0c}$ correspond to the instant when the EATS reaches the center of the jet for $R = R_0$ and $R = R_f$, respectively. These two angular timescales are relevant for polarization curves for B_{tor} in the top panel. See Table 1 and caption of Fig. 1 for definition of various symbols.

over the duration of the pulse in both the on-beam and off-beam cases, whereas both the B_{\perp} and B_{\parallel} fields only show a single 90° change in the PA in the on-beam case; no such PA change occurs in the off-beam case. The polarization abruptly vanishes at $\tilde{t} = \tilde{t}_{f+}$ when the flux vanishes. A noteworthy point is that some of the interesting behavior, e.g. the change in PA, occurs deep in the tail of the pulse profile when high-latitude emission dominates. At this point, the decline in flux is so severe that it renders detecting these changes in Π very challenging. This is less of an issue for the scenario shown in the bottom panel. In this case the symmetry breaking timescale $\tilde{t}_{0-} < \tilde{t}_f$, and therefore, $|\Pi| > 0$ can be measured for both the B_{\perp} and B_{\parallel} fields near the pulse peak and thereafter. Still, the degree of polarization reaches a more appreciable value only during the tail of the pulse in the lightcurve. While for these two fields the change in PA is similar to that in the top-panel, the behaviour is different for B_{tor} which shows no PA change at all.

In the top panel, there are two additional timescales that are rel-

evant for the B_{tor} field. These are shown using a green dotted line in Fig. 6, and they correspond to the arrival time of photons from the center of the outflow at $\tilde{t} = \tilde{t}_{0c}$ and $\tilde{t} = \tilde{t}_{fc}$ when the shell is, respectively, at $R = R_0$ and $R = R_f$, where

$$\tilde{t}_{0c} = 1 + q^2 \xi_{0,j} \quad (m = 0), \quad (31)$$

$$\tilde{t}_{fc} = \tilde{t}_f + q^2 \xi_{0,j} \hat{R}_f. \quad (32)$$

For a more general m we have

$$\tilde{t}_{0c} = 1 + (1 + m)q^2 \xi_{0,j}, \quad (33)$$

$$\tilde{t}_{fc} = \tilde{t}_f + (1 + m)q^2 \xi_{0,j} \hat{R}_f.$$

These times reflect inflexion points across which the temporal behavior of the polarization curve changes. While these can be more clearly seen in the top panel, they are not that obvious in the bottom panel due to integration over larger ΔR .

The polarization ‘break’ obtained at $\tilde{t} = \tilde{t}_{0-}$ for the B_{\perp} and B_{\parallel} configurations can potentially be used to infer θ_j , the half-opening angle

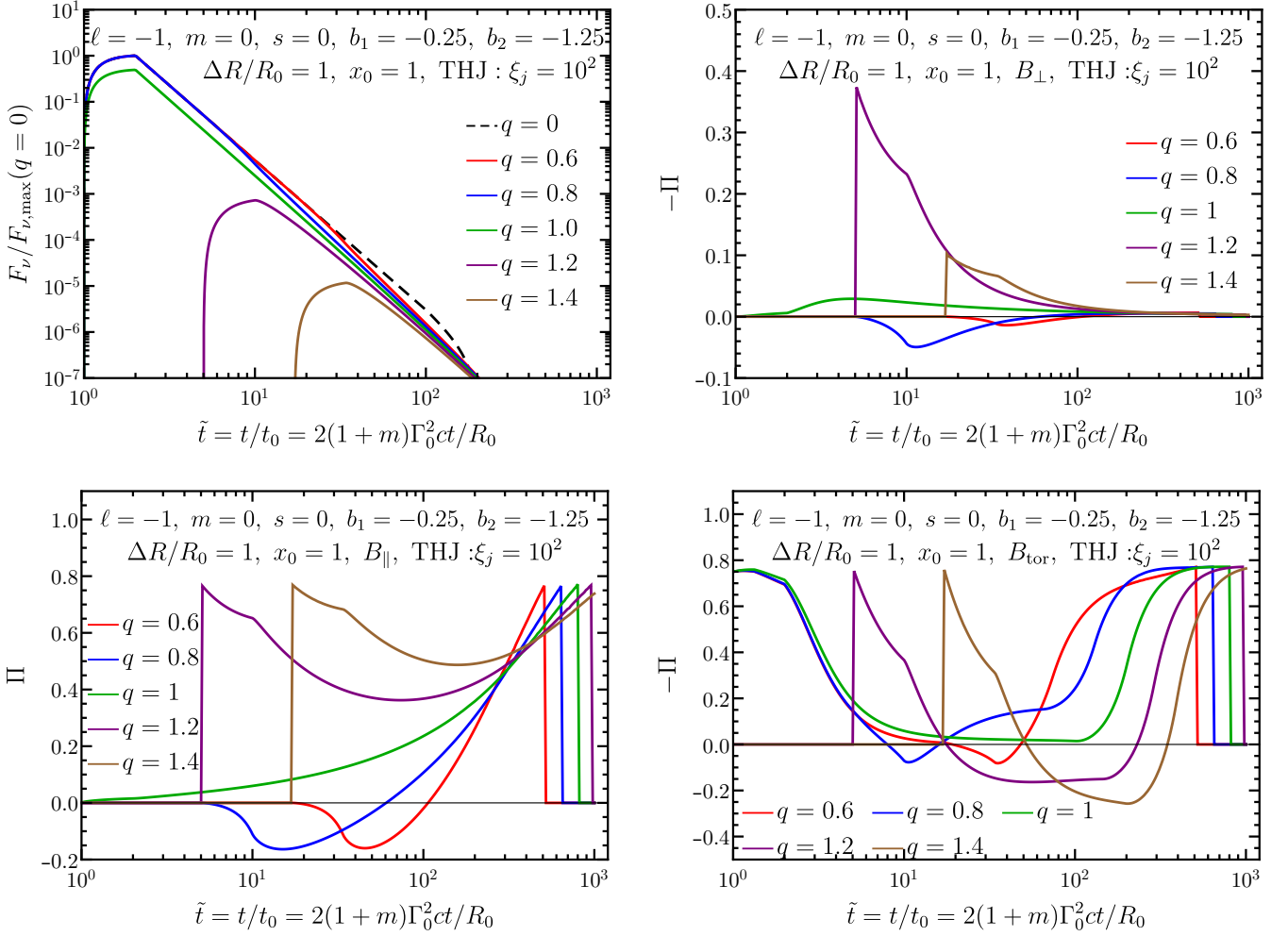


Figure 7. Pulse profile (top-left) and temporal evolution of polarization (Π) over a single pulse shown for different magnetic field configurations and for different viewing angles $q = \theta_{\text{obs}}/\theta_j$. The outflow profile is that of a KED flow with geometry of a top-hat jet (THJ) with $\xi_j = (\Gamma\theta_j)^2 = 100$. Similar results are obtained for a PFD flow. See Table 1 and caption of Fig. 1 for definition of various symbols.

of the jet, if Γ can be estimated independently from, e.g. high-energy spectral cutoff due to $\gamma\gamma$ -annihilation (e.g., [Granot et al. 2008](#); [Gill & Granot 2018](#)). In total there are four unknowns, namely θ_{obs} , θ_j , Γ , and the spectral index, where the first three combine to form two variables q and ξ_j that can be constrained using polarization while the spectral index is obtained from the observed spectrum. The polarization break time provides one constraint and the pulse-integrated polarization, which depends on both q and ξ_j , provides another. Of course, in practice this is a challenging exercise since it requires an extremely bright GRB that shows a single pulse over which high signal-to-noise measurements for the polarization are obtained.

In the top-left panel of Figure 7, we show the pulse profiles for different viewing angles normalized by $F_{\nu,\text{max}}$ at $q = 0$, the pulse profile for which is shown with a black dashed line. The $q = 0$ observer receives photons from both edges of the jet at the same time at $\tilde{t} = \tilde{t}_{0-} = \tilde{t}_{0+}$, and the deficit in flux can be seen at $\tilde{t} = 1 + (1+m)\xi_{0,j} = 101$ for $\xi_{0,j} = 100$ and $m = 0$. When $q < 1 - \xi_j^{-1/2}$ the pulse profiles overlap with that for $q = 0$ until $\tilde{t} = \tilde{t}_{0-}(q)$ due to missing emission. For $q > 1 - \xi_j^{-1/2}$ the instant at which a deficit in flux occurs moves to smaller times until $q = 1$, when the observer's LOS is directly along the edge of the jet. In this case, the deficit in

flux becomes precisely by half and it is apparent from $\tilde{t} = 1$ since the edge of the jet is visible to the observer from the arrival time of the very first photons. The arrival time of the first photons shifts to $\tilde{t}_{0-} > 1$ for $q > 1$ and the flux normalization also declines very rapidly with q since the emission is coming from higher latitudes. The suppression in flux is particularly severe for a top-hat jet for $q > 1 + \xi_j^{-1/2}$ which means that distant GRBs are always observed through (at least nearly) on-beam emission, $q \lesssim 1 + \xi_j^{-1/2}$. In addition, the width of the pulse for off-beam emission also increases in comparison to that for on-beam emission, such that

$$\frac{\Delta t_{\text{off}}}{\Delta t_{\text{on}}} = \frac{t_{0-}}{t_0} = \tilde{t}_{0-} = 1 + (1+m)(1-q)^2 \xi_{0,j}. \quad (34)$$

The other panels of Figure 7 show the temporal evolution of polarization for different B-field configurations. The polarization curves are broadly similar for the B_{\perp} and B_{\parallel} configurations, with the only difference being the high level of polarization for the latter case due to the field being ordered in the radial direction as compared to it being random in the plane transverse to the radial direction, which also reflects in an opposite sign of the polarization (i.e. a 90° difference in the PA). The feature that is common to polarization curves of both B_{\perp} and B_{\parallel} cases is that when $q < 1$ the smaller the q the later the oc-

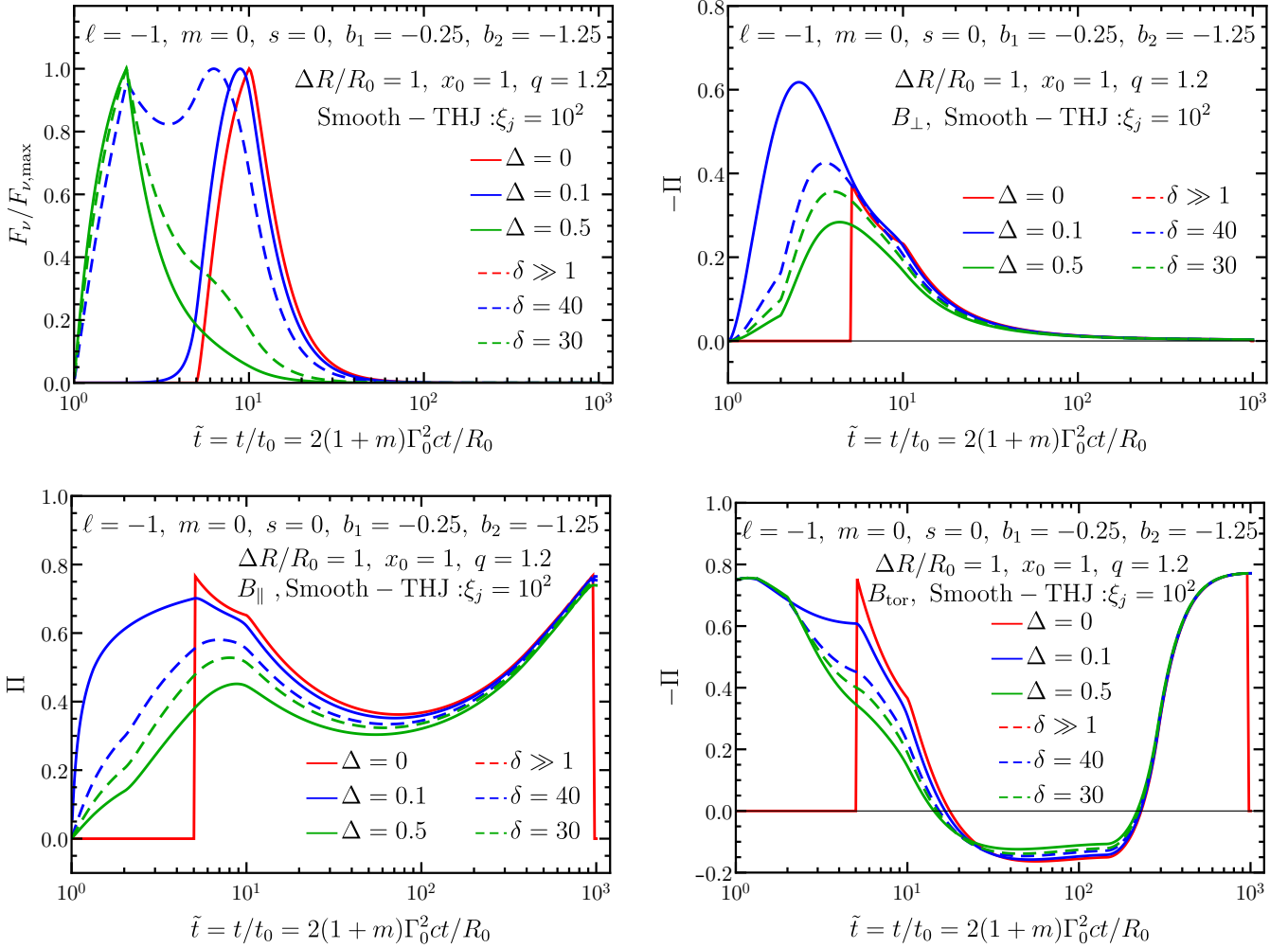


Figure 8. Pulse profile (top-left) and temporal evolution of polarization over a single pulse shown for a smooth top-hat jet (uniform core and decaying profile of L'_ν for $\theta > \theta_j$) for different smoothing parameter Δ (δ) for an exponential (power-law decay; see Eq. 35 & 36). Polarization curves are shown for random B_\perp (top-right), B_\parallel (bottom-left), and B_{tor} (bottom-right) fields. See Table 1 and caption of Fig. 1 for definition of various symbols.

currence of the polarization break and the lower the maximum level of polarization. Therefore, as argued in e.g. Gill et al. (2020a) using pulse-integrated polarization, most GRBs with such field configurations will not show any discernible levels of polarization, unless the outflow has a B_{tor} field or a locally ordered field when emission comes from incoherent patches (or more generally, a field ordered on angular scales $\gtrsim 1/\Gamma$).

In the case of a B_{tor} field, the polarization evolution is completely different from that obtained for the B_\perp and B_\parallel fields. Not only the polarization is always maximal at the start of the emission for all q values, it also shows two 90° changes in the PA in all cases except for $q = 1$. Of course, the second flip will be very difficult to detect as it always occurs deep in the tail of the pulse. The abrupt drop in flux at $\tilde{t} = \tilde{t}_{f+}$ simply reflects the instance when the last photons are received from the flow.

4.3 Polarization from a uniform jet with smooth edges

The top-hat jet geometry is an idealization of the narrowly beamed relativistic outflow in GRBs. In reality, the jet can have *smooth* edges both in comoving emissivity and bulk Γ . Such flows are referred to

as structured jets. Here, for simplicity, we only consider a smooth top-hat jet for which the comoving emissivity is uniform in the core and drops off either exponentially with some smoothing factor Δ for polar angles $\theta > \theta_j \Leftrightarrow \xi_0 > \xi_{0,j}$, such that

$$f_{\text{exp}}(\theta) = \begin{cases} 1, & \xi_0 \leq \xi_{0,j} \\ \exp\left(-\frac{\sqrt{\xi_{0,j}} - \sqrt{\xi_0}}{\Delta}\right), & \xi_0 > \xi_{0,j}, \end{cases} \quad (35)$$

or as a power law with smoothing factor δ with

$$f_{\text{pl}}(\theta) = \begin{cases} 1, & \xi_0 \leq \xi_{0,j} \\ \left(\frac{\xi_0}{\xi_{0,j}}\right)^{-\delta/2}, & \xi_0 > \xi_{0,j}, \end{cases} \quad (36)$$

while the bulk Γ is uniform everywhere.

In a flow where the bulk- Γ also depends on the polar angle θ , the temporal evolution of polarization will be significantly affected. Similar to the comoving emissivity, a typical and physically motivated assumption is that Γ also decreases away from the jet-symmetry axis with θ . In that case, the angular size of the beaming cone, $\sim \Gamma^{-1}$, must grow with θ , which means that observers with $q > 1$ that were significantly off-beam should now be able to see

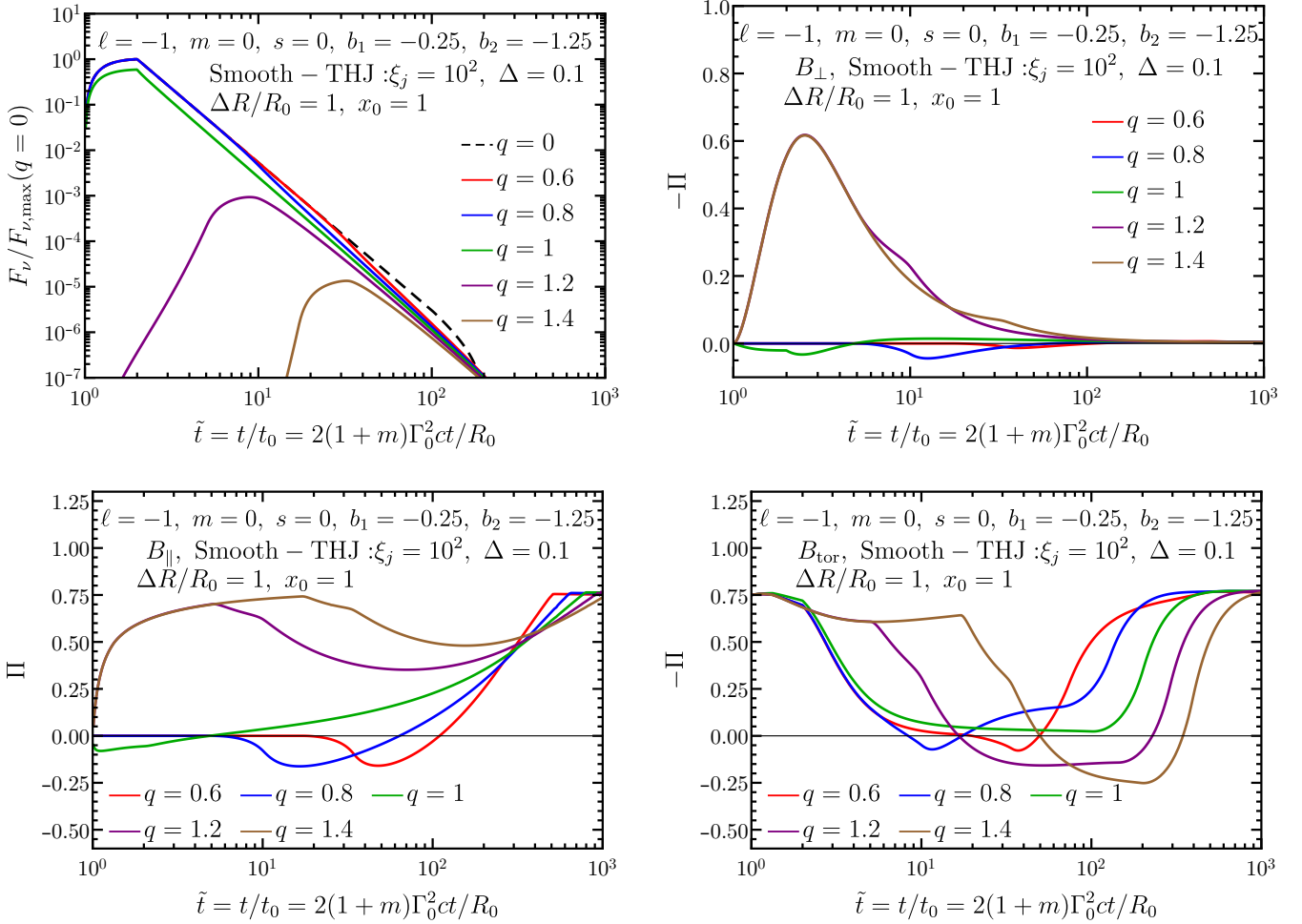


Figure 9. Pulse profile (top-left) and temporal evolution of polarization over a single pulse shown for a smooth top-hat jet (uniform core and exponentially decaying wings in L'_{ν}) with random B_{\perp} (top-right), B_{\parallel} (bottom-left), and B_{tor} (bottom-right) for different $q = \theta_{\text{obs}}/\theta_j$. See Table 1 and caption of Fig. 1 for definition of various symbols.

brighter regions at $\theta < \theta_{\text{obs}}$. Not only that, the EATS is strongly modified due to the angular structure of Γ and as a result the two-dimensional cross-sections of the EATS shown in Fig. 4 for a uniform jet don't hold. Bulk- Γ angular profiles that drop off steeply with θ yield larger polarization than shallower ones (see, e.g., Gill et al. 2020a). Further discussion of these complexities are out of the scope of the present work and will be presented in a future work. Pulse-integrated polarization curves as a function of q and for both smooth top-hat jets as well as structured jets are given in Gill et al. (2020a).

In Fig. 8 we show the pulse profile (top-left panel) and polarization curves for $q = 1.2$ and for different levels of smoothing with $\Delta > 0$ ($\delta = \text{few} \times 10$) for a smooth top-hat jet with exponential (power-law) wings; $\Delta = 0$ and $\delta \gg 1$ yields a top-hat jet with sharp edges. As the jet is made smoother the amount of flux along the observer's LOS gradually increases since now there is non-vanishing emissivity at $\theta_{\text{obs}} > \theta_j$ for sufficiently smoother profiles, which means that the observer can receive on-beam emission. As a result, when Δ (δ) increases (decreases) the arrival time of first photons emitted at $R = R_0$ becomes dominated by the radial time delay while the angular delay becomes smaller. Correspondingly, the pulse now shows non-vanishing polarization at $\tilde{t} < \tilde{t}_{0-}$. In general, the shape of the polar-

ization curve is similar to that obtained for a top-hat geometry, but now only smoother and/or broader. In the case of a smooth power-law wing, the pulse profile in some cases shows two peaks/bumps where the second bump at $\tilde{t} > \tilde{t}_f$ becomes increasingly dominant for larger values of δ (therefore sharper edged jets).

In Fig. 9 we again show the pulse profiles and polarization curves, now for a fixed $\Delta = 0.1$ and different values of q . This figure should be compared with Fig. 7 with which it shares many features. The pulse profiles still show a deficit in flux after the nearer edge first becomes visible, but the off-beam emission pulses now show a shallower rise to the pulse peak due to the structure of the outflow. In addition, the peak of the curve corresponding to $q = 1$ normalized by that obtained for $q = 0$ is now larger than half, again due to the angular structure of the jet that contributes additional flux. The polarization curves with $q < 1$ show a similar trend as before for all the field configurations, but the $q = 1$ case now shows a 90° change in PA for both the B_{\perp} and B_{\parallel} fields. In contrast with the top-hat jet case, where the polarization abruptly vanishes due to vanishing flux, the polarization curves for a smooth top-hat jet and for the B_{\parallel} and B_{tor} fields now show a plateau at the maximum level after the whole uniform core comes into view, i.e. at $\tilde{t} > \tilde{t}_{f+}$ (but the flux is vanishingly

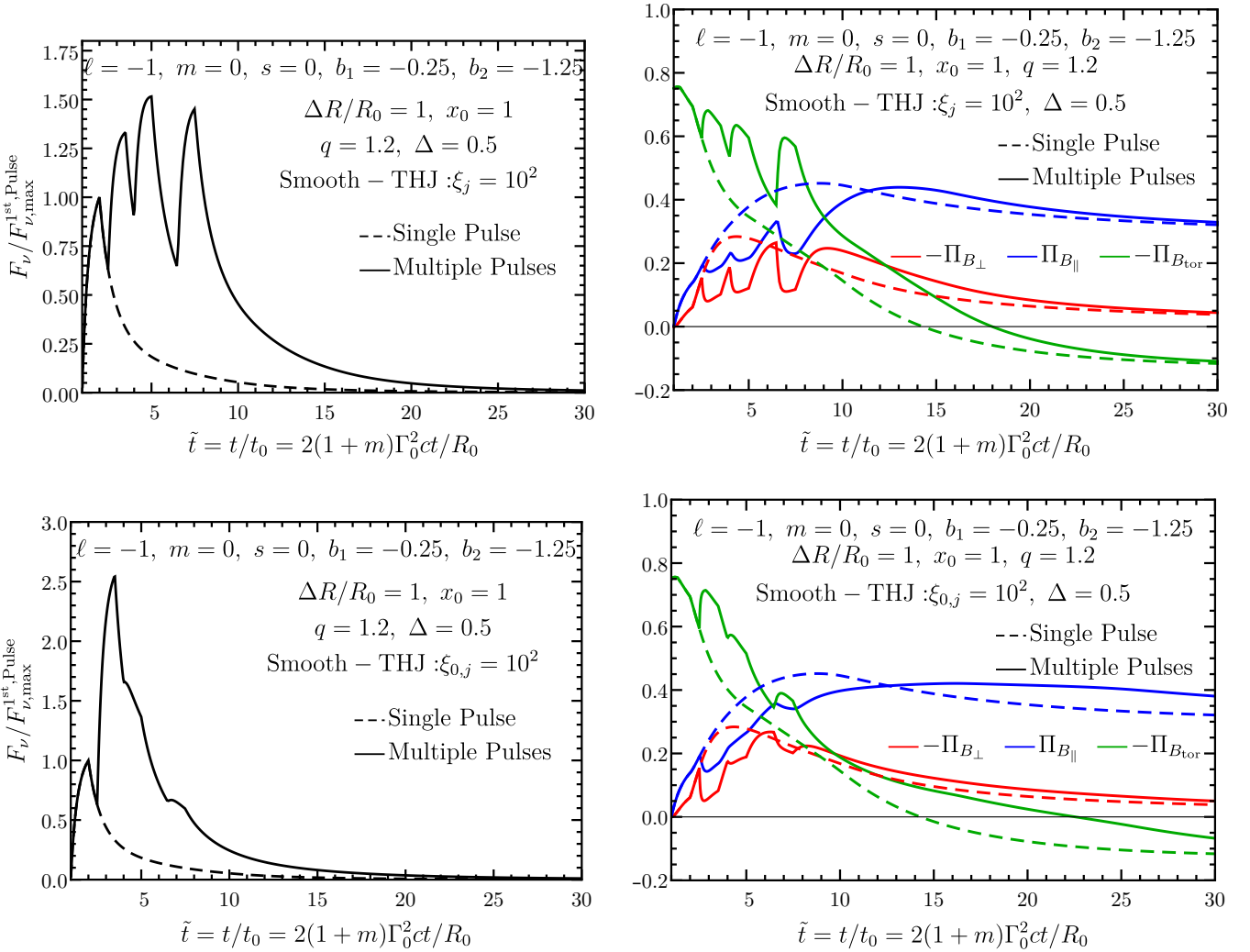


Figure 10. Pulse profile (top-left; normalized by $F_{\nu, \max}$ of the first pulse) and temporal evolution of polarization over multiple pulses (top-right) shown for a KED smooth top-hat jet (uniform core and exponentially decaying wings in L'_j) with different B-field configurations. The pulses are temporally separated due to different ejection times of multiple thin shells from the central engine. In the top-row the bulk- Γ of the shells is kept the same whereas in the bottom row shells have different bulk- Γ with the i^{th} shell having $\Gamma_{0,i} = \lambda_i \Gamma_0$, and correspondingly $\xi_{j,i} = \lambda_i^2 \xi_{0,j}$, with $\lambda_i = 1, 0.8, 1.2, 1.5$. See Table 1 and caption of Fig. 1 for definition of various symbols.

small so deep into the tail of the pulse making it extremely difficult to measure such a polarization plateau).

5 LINEAR POLARIZATION OVER MULTIPLE PULSES

GRB observations are typically photon starved unless the source is particularly bright or relatively nearby. This presents a challenge for polarization measurements that require high photon counts to be able to yield statistically significant results. To increase the number of photons integration over multiple pulses is generally performed, which alters the polarization evolution from what is expected for a single pulse. Here we consider multiple pulses that originate due to episodic internal dissipation in the relativistic flow as it expands. In the case of internal shocks, this can occur due to the intermittent ejection of multiple shells by the central engine that collide at different radii. On the other hand, a Poynting flux dominated flow can

suffer multiple dissipation episodes due to magnetic reconnection of a stochastic magnetic field and/or MHD instabilities.

To describe the pulse structure and linear polarization from multiple pulses, the same formalism as described earlier for a single pulse can be used. Here we follow the formalism introduced in Genet & Granot (2009) to describe multiple pulses. In a KED flow, the pulses are now separated temporally due to ejection of multiple shells that have different ejection times $t_{\text{ej},z} = t_{\text{ej}}/(1+z)$, such that the onset of the i^{th} pulse is given by $t_{\text{onset},z} = t_{\text{ej},z,i} + t_{0,z,i}$. Variation in emission radii and bulk Γ for the different shells can change $t_{0,z,i} = R_{0,i}/2(1+m)\Gamma_{0,i}^2 c$ as well as having different $(\Delta R)_i/R_{0,i}$, resulting in varied $t_{f,z,i} = t_{0,z,i}[1 + (\Delta R)_i/R_{0,i}]$, can lead to a variety of pulse structures. For simplicity, here we fix $R_{0,i} = R_0$, $(\Delta R)_i = \Delta R$, and θ_j for all the pulses, where it's understood that θ_{obs} cannot change between the different pulses. We allow Γ to vary, such that $\Gamma_{0,i} = \lambda_i \Gamma_0$ where we define the bulk Γ of the first pulse $\Gamma_{0,1} = \Gamma_0$, which yields $\tilde{t}_{0,i} \equiv t_{0,z,i}/t_{0,z,1} = t_{0,z,i}/t_0 = \lambda_i^{-2}$. Finally, the onset and peak times of the i^{th} pulse normalized by the onset time of the first pulse, $t_{0,z,1} = t_0$,

is

$$\tilde{t}_{\text{onset},i} = \tilde{t}_{\text{ej},i} + \lambda_i^{-2} \quad (37)$$

$$\tilde{t}_{\text{peak},i} = \tilde{t}_{\text{ej},i} + \lambda_i^{-2}(1 + \Delta R/R_0). \quad (38)$$

We note that the peak times of the subsequent pulses after the first one can be different from $\tilde{t}_{\text{peak},i}$ due to overlapping flux of neighbouring pulses.

In Fig. 10, we show the pulse profiles (left-panel) for multiple pulses and the corresponding polarization (right-panel) for a KED smooth top-hat jet with three different magnetic field configurations. The single pulse case is also shown for comparison and to isolate the effect of having multiple pulses on polarization. In the top row we consider pulses with the same fixed bulk Γ , i.e. $\lambda_i = 1$, for which the different timescales are: $\tilde{t}_{\text{ej},i} = 0, 1.5, 3, 5.5$, and $\tilde{t}_{\text{onset},i} = \tilde{t}_{\text{ej},i} + 1 = 1, 2.5, 4, 6.5$. In the bottom row different pulses have different $\Gamma_{0,i}$, with $\lambda_i = 1, 0.8, 1.2, 1.5$ and $\tilde{t}_{\text{ej},i} = 0, 0.94, 3.3, 6.1$, which yields the same onset time as for the $\lambda_i = 1$ case. For incoherent radiation the Stokes parameters are additive, and therefore the polarization at any given time is obtained from

$$\Pi(\tilde{t}) = \frac{\sum_i Q_i(\tilde{t})}{\sum_i I_i(\tilde{t})}, \quad (39)$$

where I_i and Q_i are the Stokes parameters for the individual pulses. Here again, due to symmetry, $U_i(\tilde{t}) = 0$. The polarization evolution also shows multiple spikes, mirroring the behavior of the lightcurve. This occurs due to the fact that the increase in total intensity $I(\tilde{t})$ is not matched equally with the increase in the polarized intensity $Q(\tilde{t})$ as contribution from other pulses are added. As a result, a sharp drop in polarization occurs at the time of the onset of the next pulse. The late-time level of polarization, however, coincides with that obtained for a single pulse when $\lambda_i = 1$. Here we have only explored a scenario where all the pulses have the same properties except variation in bulk Γ . A variety of pulse shapes (see, e.g., Genet & Granot 2009), and their corresponding polarization curves, due to variations in peak intensity, duration, as well as the spectrum can be produced using the given formalism in a straightforward manner. In order to observe these rapid changes in polarization a very bright GRB as well as a sensitive gamma-ray polarimeter that can obtain such time-resolved observations is needed. The latter requirement is still not feasible and therefore when integration is carried out over multiple pulses it becomes critical that measurements are compared with theoretical models that account for multiple pulses.

When time integration is performed, whether over a single bright pulse or over an emission episode comprising of multiple pulses, it is equally critical to compare the measurements with time-integrated model predictions. Time-integrated polarization over a temporal segment $\tilde{t}_1 < \tilde{t} < \tilde{t}_2$ is obtained from

$$\Pi(\tilde{t}_1, \tilde{t}_2) = \frac{\int_{\tilde{t}_1}^{\tilde{t}_2} Q(\tilde{t}) d\tilde{t}}{\int_{\tilde{t}_1}^{\tilde{t}_2} I(\tilde{t}) d\tilde{t}}. \quad (40)$$

In Fig. 11, we show the time-integrated polarization for a smooth top-hat jet with B_{tor} field. Two cases are highlighted, one comprising of a single pulse and the other with multiple pulses. In both, the time-integrated polarization is significantly different, as should be expected, from the instantaneous polarization within the temporal segment. The 90° change in PA can still be obtained in this particular case, however, with an obvious side-effect that time-integration washes out the information on the exact time when the PA changes relative to the arrival time of the first photons.

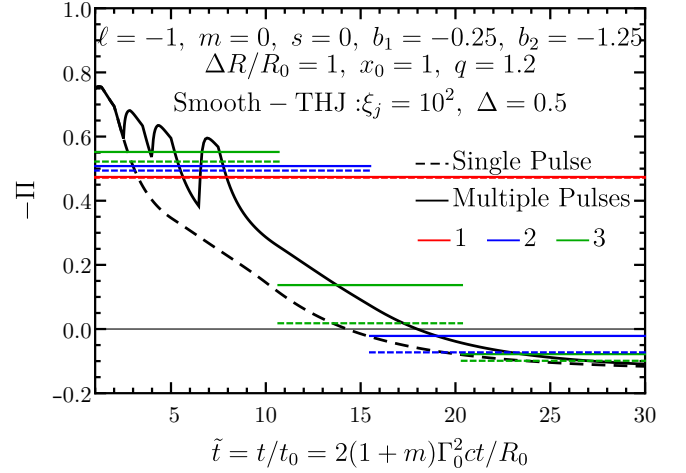


Figure 11. Time-integrated polarization for a KED smooth top-hat jet (uniform core and exponentially decaying wings in L'_ν) with B_{tor} field and with bulk- Γ the same for different pulses. Temporal segments over which polarization is obtained are calculated by dividing the pulse into one (red), two (blue), or three (green) part(s). The assumed parameters are the same as in the top row of Fig. 10. See Table 1 and caption of Fig. 1 for definition of various symbols.

6 SUMMARY & DISCUSSION

The temporal dependence of linear polarization in GRB prompt emission is an important tool that can elucidate the composition and structure of ultrarelativistic flows that power GRBs and, when synchrotron emission is dominant, help us understand the magnetic field configuration in the emission region. In this work, we present a comprehensive treatment of time-resolved polarization of synchrotron emission from different magnetic field configurations, jet structures, and outflow compositions with different dynamics.

In particular, we consider a kinetic-energy-dominated (KED) flow, in which internal shocks efficiently dissipate the kinetic energy of baryons when the flow is coasting, and a Poynting-flux-dominated (PFD) flow, where magnetic energy is dissipated due to magnetic reconnection or MHD instabilities which also accelerates the flow. The pulse profiles and polarization curves are calculated for a radially expanding ultrarelativistic (with bulk $\Gamma \gg 1$) thin outflow that continuously radiates over radii $R_0 \leq R \leq R_0 + \Delta R$. Both of these are broadly similar for the two outflows. The main difference between the two cases can be attributed to the fact that the PFD flow is accelerating, with $\Gamma \propto R^{1/3}$, which causes all critical timescales, including the width of the pulses, to become shorter in comparison to a KED flow.

In both types of outflows power-law electrons gyrating in either shock-generated small-scale or globally ordered large-scale magnetic fields produce synchrotron emission. In a KED flow, the magnetic field configuration, in general, can resemble a tangled field that lies entirely in the plane transverse to the radial direction (B_\perp) or an ordered field aligned with the radial direction (B_\parallel) at every point of the outflow. We note that although B_\perp is considered in many works as it's physically motivated, achieving such an anisotropic field configuration in reality may be challenging (see, e.g., the discussion in Gill & Granot 2020, for shock-generated field structure in relativistic collisionless shocks). Moreover, B_\parallel is likely even harder to achieve physically, its main appeal for a shock produced field being that it is

(trivially) symmetric w.r.t the local shock normal. For a PFD flow, the most relevant field configuration is that of an ordered toroidal field (B_{tor}), although other global field configurations are possible, and significant magnetic reconnection can create a substantial field component that has random orientations on small angular scales. Alternatively, it's possible that the emission region is pervaded by a locally ordered field whose coherence length is similar to or larger than the angular size of the beaming cone, such that $\theta_B \gtrsim 1/\Gamma$. For observers with viewing angle $\theta_{\text{obs}} = 0$ only the locally ordered field would yield non-vanishing polarization. All the other field configurations considered here, which are all axisymmetric, require the observer to have $\theta_{\text{obs}} > 0$ and for the B_{\perp} and B_{\parallel} fields the flow to be inhomogeneous in some way to break the symmetry and yield net non-zero polarization.

The symmetry is broken by means of the uniform flow either having a sharp edge (at $\theta = \theta_j$), as in a narrowly beamed top-hat jet, or a smooth edge, as in a smooth top-hat jet with smoothly decaying emissivity wings outside of the uniform narrow core, and the observer having $q \equiv \theta_{\text{obs}}/\theta_j > 0$. Magnetic field configurations in which the polarization vectors are symmetric around the observer's LOS, e.g. B_{\perp} and B_{\parallel} , the polarization only begins to grow when the observer first 'sees' the edge of the jet nearer to their LOS. The time at which this happens, $\tilde{t} = \tilde{t}_{0-}$ (see Eq. 29), is exactly the same when the received emission is on-beam ($q < 1 + \xi_{0,j}^{-1/2}$) or off-beam ($q > 1 + \xi_{0,j}^{-1/2}$) from a narrowly beamed top-hat jet with $\xi_{0,j} \equiv (\Gamma_0 \theta_j)^2 \gg 1$. In the case of off-beam emission this time also marks the arrival time of the first photons, however, since the flux is dominated by high latitude emission, the GRB becomes too dim making it harder to reliably detect any polarization.

In a top-hat jet, the three magnetic field configurations, namely B_{\perp} , B_{\parallel} , and B_{tor} , show distinct polarization evolution over a single pulse with some common features. For an on-beam observer both B_{\perp} and B_{\parallel} always show a 90° change in PA, but the B_{tor} field case either shows two such changes over the pulse duration or none depending on ξ_j , $\Delta R/R_0$, and q . When the received emission is off-beam, only the B_{tor} shows 90° PA changes whereas both B_{\perp} and B_{\parallel} fields show a steady PA.

In a smooth top-hat jet, the general features of the polarization curves as obtained for the top-hat jet still remain. As the jet becomes more smooth in emissivity around the edges, by developing e.g. exponentially/power-law decaying wings, the observer starts receiving on-beam emission now that there's some material that emits along the LOS. Therefore, significantly high levels of polarization are obtained for $q > 1 + \xi_{0,j}^{-1/2}$ in a smooth top-hat jet at $\tilde{t} < \tilde{t}_{0-}$ when there was none in the case of a top-hat jet.

Due to the paucity of γ -ray photons, time-integration over smaller (compared to pulse duration) temporal segments of a bright single pulse or an emission episode comprising of multiple pulses is routinely performed to gain high signal-to-noise measurements. We show how multiple pulses can be modeled using the same single pulse framework and how their polarization can be obtained. In the case of a single bright pulse, time-integrated polarization over several temporal segments yields a coarse trend that can only be interpreted accurately by modeling the time-resolved polarization for a given field configuration and outflow dynamic and structure. The same is true for multiple pulses.

Below we collect the main points of this work:

- In a top-hat jet, when $q = \theta_{\text{obs}}/\theta_j < 1$, an ordered B-field, e.g. B_{tor} , always yields the highest polarization ($\Pi \lesssim 75\%$) over most of the pulse duration starting from the arrival time of the first photon.
- For the B_{\perp} and B_{\parallel} fields $\Pi = 0$ until the observer sees the nearest

edge of the jet at $\tilde{t} = \tilde{t}_{0-}$. Then the polarization grows to $\Pi \lesssim 15\%$ before the low flux level in the pulse tail makes it challenging to measure even higher Π values, especially for B_{\parallel} where Π is highest deep in the pulse tail.

- All three B-field cases show a 90° change in PA, sometimes even twice over the pulse duration for the B_{tor} case. The PA can only change by 90° if the global flow and magnetic field configuration is axisymmetric. Furthermore, the PA only changes in the pulse tail for all three field configurations which makes it difficult to measure.

- For $q > 1$ high Π can be measured for the three field configurations right from the start of the pulse. However, the fluence sharply drops with q for $q > 1$, making such measurements challenging.

- Pulse-integrated polarization is significantly different from time-resolved polarization, both when the emission consists of a truly single pulse or multiple overlapping pulses. Therefore, time-resolved measurements should only be compared with time-resolved theoretical models.

6.1 Time-Varying Polarization Angle

Most measurements of prompt GRB polarization report a fixed PA (see, e.g., Table 1 in Gill et al. 2020a, and references therein). In many cases, this may simply be a result of integrating over the entire pulse, which naturally gives a single PA, and not carrying out a time-resolved analysis due to low photon counts. Where the latter has been possible, albeit only for a few GRBs, a change in PA was noted. A change in PA was reported for *IKAROS*-GAP detected GRB 100826A (Yonetoku et al. 2011) where the prompt emission was divided into two ~ 50 s intervals, each containing multiple spikes, with the two intervals having polarization $\Pi_1 = 25 \pm 15$ per cent and $\Pi_2 = 31 \pm 21$ per cent and PAs $\phi_1 = 159^\circ \pm 18^\circ$ and $\phi_2 = 75^\circ \pm 20^\circ$. Time-resolved analysis of a single pulse GRB 170114A detected by POLAR showed a large change in PA between two 2 s intervals with $\phi_1 = 122^\circ$ and $\phi_2 = 17^\circ$ (Zhang et al. 2019). A more refined time-resolved analysis (Burgess et al. 2019) that simultaneously fitted both the spectrum and polarization for the same GRB showed a gradual change in PA over the pulse while the polarization showed an increase towards the peak of the pulse reaching levels of $\Pi \sim 30$ per cent at the peak. Chand et al. (2019) reported an energy dependent gradually changing polarization and PA for GRB 171010A but the statistical significance of the polarization was low ($\lesssim 2.5\sigma$). A varying degree of polarization and PA was also reported in Sharma et al. (2019) for GRB 160821A that was observed by multiple instruments, namely *Fermi*-GBM/LAT, *AstroSat*-CZTI, and *Swift*-BAT. The polarization was obtained in three time intervals and it remained high with $\Pi_1 = 71^{+29}_{-41}$ per cent, $\Pi_2 = 58^{+29}_{-30}$ per cent, and $\Pi_3 = 61^{+39}_{-46}$ per cent with detection significance for all intervals between $\sim 3\sigma$ and $\sim 4\sigma$. The PA showed a remarkable evolution where it changed by $\Delta\phi_{1,2} = 81^\circ \pm 13^\circ$ and $\Delta\phi_{2,3} = 80^\circ \pm 19^\circ$.

For the magnetic field configurations considered in this work, the polarization angle can only change exactly by $\Delta\phi = 90^\circ$ and a gradual change of the PA is not possible. There are tantalizing hints of a 90° change in the PA in some of the GRBs, as discussed above, but the results are not yet conclusive. The result presented by Sharma et al. (2019) where the PA changes by 90° twice over the emission is again very exciting as such a change over a single pulse can only occur for the B_{tor} field configuration. The only difficulty, according to the modeling done here, is that both 90° changes occur in the decaying tail of the pulse when high latitude emission dominates the flux. In the measurement presented by Sharma et al. (2019) the PA shows a change close to the peak of the emission. Another scenario in which a 90° PA change can be obtained includes contribu-

tion from multiple pulses and when the LOS is close to the edge of the jet, such that $\theta_{\text{obs}} \approx \theta_j$, along with a change in bulk Γ between the pulses which would change $\xi_j = (\Gamma\theta_j)^2$. Alternatively, such a change in the PA can be obtained due to magnetic reconnection, e.g. in the ICMART model (Zhang & Yan 2011), where the local magnetic field orientation, which is orthogonal to the wave vector of the emitted photon, itself changes by 90° as the field lines are destroyed and reconnected in the emission region (Deng et al. 2016). To obtain a change in the PA other than $\Delta\phi = 90^\circ$ or to get a gradually changing PA the condition for axisymmetry must be relaxed and the magnetic field configuration or orientation in the emission region must change. One possibility is that if the different pulses that contribute to the emission arise in a ‘mini-jet’ within the outflow (e.g., Shaviv & Dar 1995; Lyutikov & Blandford 2003; Kumar & Narayan 2009; Lazar et al. 2009; Narayan & Kumar 2009; Zhang & Yan 2011). In this case the different directions of the mini-jets or bright patches w.r.t. the LOS (e.g. Granot & Königl 2003; Nakar & Oren 2004) would cause the PA to also be different between the pulses even for a field that is locally symmetric w.r.t the local radial direction (e.g. B_\perp or B_\parallel) as well as for fields that are axisymmetric w.r.t to the center of each mini-jet (e.g. a local B_{tor} for each mini-jet). Finally, broadly similar result would follow from an ordered field within each mini-jet (B_{ord}) which are incoherent between different mini-jets. Time-resolved measurement in such a case would naturally yield a time-varying PA. Alternatively, as shown by Granot & Königl (2003) for GRB afterglow polarization, a combination of an ordered field component (e.g. B_{ord}) and a random field, like B_\perp , can give rise to a time-varying PA between different pulses that, e.g., arise from internal shocks. The ordered field component here would be that advected from the central engine and the random field component can be argued to be shock-generated. Notice that the ordered field component should not be axisymmetric in order for the position angle to smoothly vary.

6.2 Energy-Dependent Polarization

As we showed in this work, using a thin spherical shell and band-function spectrum that evolves with radius, polarization at any given time is energy dependent. In the case of pure synchrotron emission the spectrum would move across the instrument’s energy window towards lower energies due to spectral softening caused by the radial evolution of the spectral peak energy. This softening can be inferred from Eq. (18) where setting $x = 1$ would yield the temporal evolution of the spectral peak, such that $x_0 \equiv \nu/\nu_0 = \tilde{t}^{(2d-m)/2(1+m)}$, which for $m = 0$ yields $x_0 = \tilde{t}^d$ where $d = -1$ for a KED flow. Consequently, the level of polarization at a fixed observed energy would change not only due to its temporal evolution, as in an infinite power-law spectrum, but also due to the drift of the spectral peak since the synchrotron polarization depends on the local spectral index.

Energy dependent polarization is a powerful tool particularly when multiple spectral components are present. These can arise, e.g., in photospheric emission models where the peak of the spectrum may be dominated by a quasi-thermal component while a non-thermal spectrum develops both below and above the spectral peak energy (see, e.g., Beloborodov & Mészáros 2017, and references therein). Detailed numerical simulations of a PFD flow in Gill et al. (2020b) showed that depending on how particles are accelerated/heated, e.g. into a power-law energy distribution or where they form a monoenergetic distribution due to distributed heating and cooling, the non-thermal component of the spectrum arises either due to synchrotron emission or Comptonization, respectively. In such a scenario, energy dependent polarization can be used to

discriminate between the two emission mechanisms. The spectral peak is expected to be unpolarized as the photons there suffer multiple Compton scatterings causing the polarization to average out nearly to zero. In the case of synchrotron emission, significant polarization is expected away from the spectral peak energy (Lundman et al. 2018). However, if Comptonization dominates the non-thermal component, again negligible polarization is expected. Detailed exploration of energy dependent polarization is deferred to future work (Gill & Granot, 2021, in prep.).

Upcoming missions, e.g. POLAR-II (Kole 2019), LEAP (McConnell & LEAP Collaboration 2016), and eXTP (in’t Zand et al. 2019), with the ability to carry out simultaneous spectropolarimetric measurements will be able to provide much needed insights into the composition of ultrarelativistic jets and radiation processes that power GRB prompt emission.

ACKNOWLEDGEMENTS

We thank the anonymous referee for useful comments. This research was supported by the ISF-NSFC joint research program (grant No. 3296/19).

DATA AVAILABILITY

The data underlying this article will be shared on reasonable request to the corresponding author.

REFERENCES

- Ackermann M., et al., 2013, *ApJ*, **763**, 71
- Band D., et al., 1993, *ApJ*, **413**, 281
- Bégué D., Pe’er A., Lyubarsky Y., 2017, *MNRAS*, **467**, 2594
- Beloborodov A. M., 2011, *ApJ*, **737**, 68
- Beloborodov A. M., Mészáros P., 2017, *Space Sci. Rev.*, **207**, 87
- Beniamini P., Giannios D., 2017, *MNRAS*, **468**, 3202
- Beniamini P., Granot J., 2016, *MNRAS*, **459**, 3635
- Burgess J. M., Kole M., Berlato F., Greiner J., Vianello G., Produit N., Li Z. H., Sun J. C., 2019, *A&A*, **627**, A105
- Chand V., et al., 2018, *ApJ*, **862**, 154
- Chand V., Chattopadhyay T., Oganessyan G., Rao A. R., Vadawale S. V., Bhattacharya D., Bhalerao V. B., Misra K., 2019, *ApJ*, **874**, 70
- Chattopadhyay T., et al., 2019, *ApJ*, **884**, 123
- Cheng K. F., Zhao X. H., Bai J. M., 2020, *MNRAS*, **498**, 3492
- Crider A., et al., 1997, *ApJ*, **479**, L39
- Daigne F., Mochkovitch R., 1998, *MNRAS*, **296**, 275
- Deng W., Zhang H., Zhang B., Li H., 2016, *ApJ*, **821**, L12
- Drenkhahn G., 2002, *A&A*, **387**, 714
- Drenkhahn G., Spruit H. C., 2002, *A&A*, **391**, 1141
- Fishman G. J., Meegan C. A., 1995, *ARA&A*, **33**, 415
- Genet F., Granot J., 2009, *MNRAS*, **399**, 1328
- Geng J.-J., Huang Y.-F., Wu X.-F., Zhang B., Zong H.-S., 2018, *ApJS*, **234**, 3
- Ghirlanda G., Celotti A., Ghisellini G., 2003, *A&A*, **406**, 879
- Ghisellini G., Celotti A., 1999, *ApJ*, **511**, L93
- Ghisellini G., Lazzati D., 1999, *MNRAS*, **309**, L7
- Giannios D., 2006, *A&A*, **457**, 763
- Giannios D., 2008, *A&A*, **480**, 305
- Gill R., Granot J., 2018, *MNRAS*, **475**, L1
- Gill R., Granot J., 2020, *MNRAS*, **491**, 5815
- Gill R., Thompson C., 2014, *ApJ*, **796**, 81
- Gill R., Granot J., Lyubarsky Y., 2018, *MNRAS*, **474**, 3535
- Gill R., Granot J., Kumar P., 2020a, *MNRAS*, **491**, 3343
- Gill R., Granot J., Beniamini P., 2020b, *MNRAS*, **499**, 1356

- Granot J., 2003, *ApJ*, **596**, L17
- Granot J., 2005, *ApJ*, **631**, 1022
- Granot J., 2012, *MNRAS*, **421**, 2610
- Granot J., Königl A., 2003, *ApJ*, **594**, L83
- Granot J., Taylor G. B., 2005, *ApJ*, **625**, 263
- Granot J., Cohen-Tanugi J., Silva E. d. C. e., 2008, *ApJ*, **677**, 92
- Granot J., Komissarov S. S., Spitkovsky A., 2011, *MNRAS*, **411**, 1323
- Gruzinov A., 1999, *ApJ*, **525**, L29
- Guiriec S., et al., 2011, *ApJ*, **727**, L33
- Guiriec S., et al., 2015, *ApJ*, **807**, 148
- Guiriec S., Gehrels N., McEnery J., Kouveliotou C., Hartmann D. H., 2017, *ApJ*, **846**, 138
- Guo F., Liu Y.-H., Daughton W., Li H., 2015, *ApJ*, **806**, 167
- Ito H., Nagataki S., Matsumoto J., Lee S.-H., Tolstov A., Mao J., Dainotti M., Mizuta A., 2014, *ApJ*, **789**, 159
- Kagan D., Sironi L., Cerutti B., Giannios D., 2015, *Space Sci. Rev.*, **191**, 545
- Kole M., 2019, in 36th International Cosmic Ray Conference (ICRC2019), p. 572
- Kole M., et al., 2020, arXiv e-prints, p. arXiv:2009.04871
- Komissarov S. S., 2012, *MNRAS*, **422**, 326
- Kumar P., Narayan R., 2009, *MNRAS*, **395**, 472
- Kumar P., Zhang B., 2015, *Phys. Rep.*, **561**, 1
- Laing R. A., 1980, *MNRAS*, **193**, 439
- Lan M.-X., Wu X.-F., Dai Z.-G., 2020, arXiv e-prints, p. arXiv:2008.10746
- Lazar A., Nakar E., Piran T., 2009, *ApJ*, **695**, L10
- Lazzati D., Rossi E., Ghisellini G., Rees M. J., 2004a, *MNRAS*, **347**, L1
- Lazzati D., et al., 2004b, *A&A*, **422**, 121
- Lundman C., Pe’er A., Ryde F., 2014, *MNRAS*, **440**, 3292
- Lundman C., Vurm I., Beloborodov A. M., 2018, *ApJ*, **856**, 145
- Lyubarsky Y., 2010, *ApJ*, **725**, L234
- Lyubarsky Y., Kirk J. G., 2001, *ApJ*, **547**, 437
- Lyutikov M., Blandford R., 2003, ArXiv Astrophysics e-prints,
- Lyutikov M., Pariev V. I., Blandford R. D., 2003, *ApJ*, **597**, 998
- Matzner C. D., 2003, *MNRAS*, **345**, 575
- McConnell M. L., LEAP Collaboration 2016, in Eighth Huntsville Gamma-Ray Burst Symposium. p. 4051
- McKinney J. C., Uzdensky D. A., 2012, *MNRAS*, **419**, 573
- Metzger B. D., Giannios D., Thompson T. A., Bucciantini N., Quataert E., 2011, *MNRAS*, **413**, 2031
- Nakar E., Oren Y., 2004, *ApJ*, **602**, L97
- Narayan R., Kumar P., 2009, *MNRAS*, **394**, L117
- Oganesyan G., Nava L., Ghirlanda G., Celotti A., 2017, *ApJ*, **846**, 137
- Paczynski B., Xu G., 1994, *ApJ*, **427**, 708
- Parfrey K., Giannios D., Beloborodov A. M., 2015, *MNRAS*, **446**, L61
- Parsotan T., López-Cámara D., Lazzati D., 2020, *ApJ*, **896**, 139
- Piran T., 2004, *Reviews of Modern Physics*, **76**, 1143
- Preece R. D., Briggs M. S., Mallozzi R. S., Pendleton G. N., Paciesas W. S., Band D. L., 1998, *ApJ*, **506**, L23
- Ravasio M. E., Oganesyan G., Ghirlanda G., Nava L., Ghisellini G., Pescalli A., Celotti A., 2018, *A&A*, **613**, A16
- Ravasio M. E., Ghirlanda G., Nava L., Ghisellini G., 2019, *A&A*, **625**, A60
- Rees M. J., Meszaros P., 1994, *ApJ*, **430**, L93
- Rossi E. M., Lazzati D., Salmonson J. D., Ghisellini G., 2004, *MNRAS*, **354**, 86
- Rybicki G. B., Lightman A. P., 1979, Radiative processes in astrophysics
- Ryde F., 2004, *ApJ*, **614**, 827
- Ryde F., 2005, *ApJ*, **625**, L95
- Sari R., 1999, *ApJ*, **524**, L43
- Sari R., Piran T., 1997, *ApJ*, **485**, 270
- Sari R., Piran T., Narayan R., 1998, *ApJ*, **497**, L17
- Sharma V., et al., 2019, *ApJ*, **882**, L10
- Shaviv N. J., Dar A., 1995, *ApJ*, **447**, 863
- Sironi L., Spitkovsky A., 2014, *ApJ*, **783**, L21
- Spruit H. C., Daigne F., Drenkhahn G., 2001, *A&A*, **369**, 694
- Tang Q.-W., Peng F.-K., Wang X.-Y., Tam P.-H. T., 2015, *ApJ*, **806**, 194
- Thompson C., 1994, *MNRAS*, **270**, 480
- Thompson C., Gill R., 2014, *ApJ*, **791**, 46
- Toma K., et al., 2009, *ApJ*, **698**, 1042
- Uhm Z. L., Zhang B., 2014, *Nature Physics*, **10**, 351
- Uhm Z. L., Zhang B., 2015, *ApJ*, **808**, 33
- Uhm Z. L., Zhang B., 2016, *ApJ*, **825**, 97
- Vianello G., Gill R., Granot J., Omodei N., Cohen-Tanugi J., Longo F., 2018, *ApJ*, **864**, 163
- Vurm I., Beloborodov A. M., 2016, *ApJ*, **831**, 175
- Werner G. R., Uzdensky D. A., Cerutti B., Nalewajko K., Begelman M. C., 2016, *ApJ*, **816**, L8
- Yonetoku D., et al., 2011, *ApJ*, **743**, L30
- Yonetoku D., et al., 2012, *ApJ*, **758**, L1
- Zhang B., Yan H., 2011, *ApJ*, **726**, 90
- Zhang S.-N., et al., 2019, *Nature Astronomy*, **3**, 258
- in’t Zand J. J. M., et al., 2019, *Science China Physics, Mechanics, and Astronomy*, **62**, 29506

This paper has been typeset from a \LaTeX file prepared by the author.